

1 **Regionalization of IDF Curves for Mainland China: A Comparative Evaluation of Machine**
2 **Learning versus Spatial Interpolation Techniques**

3 **Yuantian Jiang¹, Wenting Wang^{1*}, Andrew T. Fullhart², Bofu Yu³, Bo Chen⁴**

4 ¹ Department of Geographic Science, Faculty of Arts and Sciences, Beijing Normal University,
5 Zhuhai 519087, China;

6 ² School of Natural Resources and the Environment, University of Arizona, Tucson, AZ, USA;

7 ³ Australian Rivers Institute, School of Engineering and Built Environment, Griffith University,
8 Brisbane, QLD 4111, Australia;

9 ⁴ State Key Laboratory of Earth Surface Processes and Resource Ecology, Faculty of
10 Geographical Science, Beijing Normal University, Beijing 100875, China

11
12 * Corresponding author: Wenting Wang (wangwenting@bnu.edu.cn)

13
14 **Key Points:**

- 15 • Interpolation and machine learning (ML) were compared for regionalizing Intensity-
16 Duration-Frequency (IDF) curves for mainland China.
17 • With daily data, ML was able to successfully estimate sub-daily intensities, achieving
18 comparable accuracy using spatial interpolation.
19 • Regionalized IDF curves dataset were developed at 0.1 and 0.5 degrees for mainland
20 China.

21

22 Abstract

23 Regionalization of Intensity-Duration-Frequency (IDF) curves is essential for designing
24 stormwater drainage systems, especially in regions without rainfall data of high temporal
25 resolution. However, most studies have not thoroughly compared regionalization methods using
26 sub-daily site observations versus gridded daily precipitation products. The potential of machine
27 learning (ML) methods driven by daily gridded precipitation remains largely underexplored. This
28 study addresses these gaps by regionalizing the IDF curves across mainland China for durations
29 ranging between 1 and 72 hours and return periods ranging from 2 to 1,000 years. Five
30 interpolation methods based on hourly observations from 2363 stations and five machine
31 learning methods ~~using based on a~~ gridded daily dataset were tested for accuracy. Both ML and
32 traditional interpolation methods showed robust performances based on the Kling-Gupta
33 Efficiency (KGE) performance measure. The most successful interpolation method was Kriging
34 with External Drift using mean annual precipitation, with $KGE > 0.96$ for 1-hr-5-yr and 24-hr-5-yr
35 storms and $KGE > 0.84$ for 1-hr-100-yr and 24-hr-100-yr storms, while Gradient Boosting was the
36 best-performing ML model, with $KGE > 0.94$ for 1-hr-5-yr and 24-hr-5-yr storms and $KGE > 0.87$
37 for 1-hr-100-yr and 24-hr-100-yr storms. Notably, ~~even though despite~~ ML ~~using~~ daily data and
38 interpolation ~~using~~ hourly data, the ML accuracy of ML gradually improved, eventually
39 approaching or even surpassing the interpolation methods as the duration and return period
40 increased. Consequently, a regionalized dataset on IDF curves for mainland China with a spatial
41 resolution of 0.1 degrees (and optionally 0.5 degrees) was generated using the optimal ML
42 regionalization method.

43 1 Introduction

44 The intensity and frequency of extreme precipitation are projected to increase under
45 global warming in response to increased radiative forcing on the hydrologic cycle based on
46 governing physical laws, including the Clausius-Clapeyron relationship (Benestad et al., 2021;
47 Donat et al., 2016; Skliris et al., 2016). These extreme events can lead to disasters, including urban
48 flooding, flash floods, and soil erosion, resulting in significant loss of life and property damage
49 (Gao et al., 2017; Maggioni & Massari, 2019). Intensity-Duration-Frequency (IDF) curves, which
50 ~~define~~ depict the relationships ~~among between~~ rainfall intensity, duration, and frequency of
51 occurrence (or the return period), are derived from historical extreme precipitation events. They
52 play a vital role in the design of stormwater drainage systems and flood protection structures. In
53 regions susceptible to severe flooding, accurately estimating IDF curves is crucial for developing
54 infrastructure that can mitigate property damage and safeguard human lives (Simonović, 2012).

55 Extreme precipitation events are typically characterized by short duration, high intensity,
56 and considerable spatial-temporal variability. As a result, developing accurate IDF curves requires
57 station data with high spatial density and temporal resolution, such as hourly measurements
58 (Förster, 2020; Westra et al., 2014). However, the limited availability of observational stations
59 with high temporal resolution means that IDF curves can only be derived ~~from these data are~~
60 ~~only applicable to for~~ areas where such stations exist. Consequently, it is challenging to extend
61 these curves to regions lacking high-resolution precipitation records (Sangüesa et al., 2023). With
62 increased urbanization, many new water-related infrastructures will be built in areas without

63 long-term historical precipitation data. Therefore, it is crucial to regionalize and estimate IDF
64 curves for regions where high temporal resolution precipitation data is unavailable or limited.

65 Conventionally, regionalization relies on site-specific observations, with commonly used
66 methods including Regional Frequency Analysis (RFA) and spatial interpolation (Szolgay et al.,
67 2009). Regionalization of station IDFs through RFA requires identification of homogeneous
68 regions (Schlef et al., 2023). However, this process can be challenging, as defining homogeneous
69 regions often involves subjective judgment and lacks a solid physical basis (Nguyen et al., 2002).
70 As a result, the regions identified may be heterogeneous, which can negatively impact frequency
71 analysis (Halbert et al., 2016; Schlef et al., 2023). Additionally, boundary discontinuities between
72 subregions present another challenge for RFA (Zou et al., 2021).

73 Regionalization methods for IDF curves derived from ground observations also involve
74 interpolation. Two primary approaches are commonly used (Szolgay et al., 2009): (a) directly
75 interpolating the quantiles, moments, or parameters of the distribution function, followed by the
76 calculation of the distribution function for each region; or (b) first calculating the distribution
77 function at the observation stations, then interpolating the return period estimates. Research
78 conducted in the Haihe River Basin, China, for example, shows that interpolating return period
79 estimates are more accurate compared to interpolation based on distribution parameters (Yin et
80 al., 2018).

81 In terms of specific interpolation methods, researchers have frequently employed and
82 compared methods such as Inverse Distance Weighting (IDW), Ordinary Kriging (OK), and Kriging
83 with External Drift (KED). The KED method achieves higher accuracy by incorporating auxiliary
84 variables correlated with the spatial distribution of the target variable (Berndt & Haberlandt,
85 2018; Shehu et al., 2023; Yin et al., 2018). For extreme rainfall prediction, auxiliary variables such
86 as elevation and annual precipitation are correlated with the predicted variable and have the
87 potential to improve interpolation accuracy (Miao et al., 2024; Zou et al., 2021). Notably, the
88 accuracy of interpolation methods fundamentally depends on the quality of the observations. To
89 generate reliable regionalized IDF curves requires a dense observational network with long-term,
90 high-resolution data (Berndt et al., 2014; Papalexiou, 2018; Papalexiou & Koutsoyiannis, 2013;
91 Shehu et al., 2023).

92 In recent years, gridded precipitation datasets have undergone significant improvements
93 in both resolution and reliability, enhancing their potential for estimating IDF curves in regions
94 where the deployment of observational stations is challenging (Courty et al., 2019). Consequently,
95 the utilization of gridded precipitation datasets to develop IDF curves has become increasingly
96 prevalent (Ghebreyesus & Sharif, 2021; Mínguez & Herrera, 2023; Noor et al., 2021). These
97 datasets can be generated through various methods, including ground-based station
98 observations, radar, satellite data, or a combination of these sources, resulting in precipitation
99 datasets with varying temporal and spatial resolutions. Gridded IDF products can be estimated
100 using these datasets (Haruna et al., 2024; Lanciotti et al., 2022; Wambura, 2024). However,
101 estimating IDF curves involves assessing precipitation extremes, which may exhibit strong spatial
102 heterogeneity within individual grid cells of gridded—precipitation datasets. Further
103 improvements are necessary to enhance the accuracy of gridded IDF products derived from such
104 datasets (Parding et al., 2023; Schilcher et al., 2017).

105 Recent studies have explored the application of machine learning methods for
106 regionalizing IDF curves. Several studies have successfully trained machine learning models on
107 sub-daily precipitation data. For example, one study utilized Support Vector Machine to create a
108 gridded IDF dataset for Canada, while another established a gridded IDF dataset for the Qinghai-
109 Tibet Plateau using Random Forest model (Gaur et al., 2020; Ren et al., 2025). Concurrently, other
110 researches have investigated the non-stationarity of IDF curves under changing climate
111 conditions (Schlef et al., 2023; Vinod & Mahesha, 2024; Zhang et al., 2022). A key challenge in
112 this context is temporal downscaling, where some researches have employed machine learning
113 to disaggregate coarse 3-hour precipitation outputs from climate models into minute-level
114 resolution (Al Kajbaf et al., 2022; Al Kajbaf et al., 2023). This demonstrates the potential of
115 machine learning methods to produce gridded IDF datasets, which traditionally requires sub-daily
116 data, by utilizing precipitation data of a coarser temporal resolution (e.g., daily observations
117 common to rain gauges).

118 The different advantages and disadvantages of the aforementioned IDF curves
119 regionalization methods indicate that it is necessary to identify an optimal regionalization
120 method based on comparative analysis. However, most existing studies assess the accuracy of
121 regionalized IDF curves based on either a site-specific observations or grid-based datasets,
122 without comparing these two kinds of regionalization methods. Additionally, few studies have
123 evaluated the potential of applying machine learning to daily gridded precipitation datasets for
124 estimating regionalized IDF curves, including extrapolation to rainfall intensities at sub-daily time
125 intervals. Furthermore, few studies have computed regionalized IDF curves on a national scale in
126 China.

127 To address these gaps and advance IDF regionalization, this paper is structured as follows.
128 Section 2 describes the study area, data sources, and methods, including the development of IDF
129 curves, spatial interpolation techniques, machine learning approaches, and evaluation metrics.
130 Section 3 presents the results, covering station-level IDF characteristics, a comparative
131 evaluation of regionalization methods at national and regional scales, and the final regionalized
132 IDF curves. Section 4 discusses the implications of the findings, limitation of the final IDF datasets,
133 and opportunities for improvement. Finally, Section 5 summarizes the key conclusions and
134 contributions of the study.

135 **2 Data and Methods**

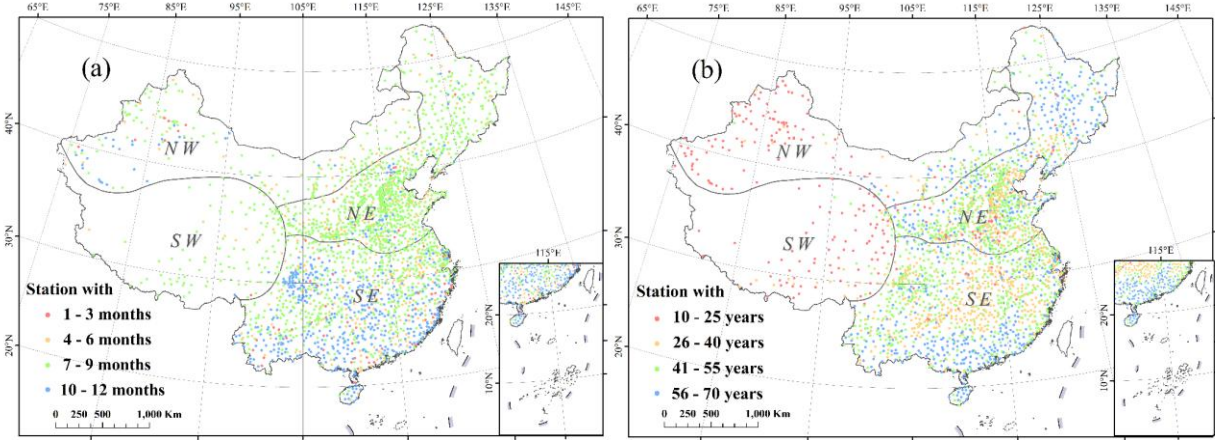
136 **2.1 Study area and data collection**

137 The study focused on the regionalization of IDF curves on a national scale in mainland
138 China. However, a method that performs well at the national level may exhibit poor accuracy in
139 specific regions. To address this, this study adopted a regionalization scheme that divides
140 mainland China into three distinct regions: the Southwestern Tibetan Plateau (SW) region, the
141 Northwestern Arid (NW) region, and the Eastern Monsoon region (Wang et al., 2019; Zhao, 1983).
142 Due to substantial internal heterogeneity within the Eastern Monsoon region, it was further
143 ~~sub~~divided into the Northeastern Monsoon (NE) sub-region and Southeastern Monsoon (SE)
144 sub-region along the Qinling-Huaihe line (Figure 1). This division reflects significant regional
145 differences in climate and topography. To provide additional regional perspective, we also

146 [evaluated model performance using an alternative division scheme based on the nine major river](#)
147 [basins of China \(Figure S3, Tables S23 to S30\).](#)

148 To regionalize IDF curves across mainland China, this study utilized two datasets: hourly
149 observations from 2363 stations in mainland China and gridded daily data from the CHM_PRE
150 (Han et al., 2023). The hourly observations were provided and quality-controlled by the National
151 Meteorological Information Center (NMIC) of the China Meteorological Administration (CMA) (Li
152 et al., 2011). Hourly data were observed by siphon self-recording rain gauges, which were not
153 operational during the cold season ~~in~~ some regions to prevent instrument failures caused by
154 low temperatures. The number of operational months for each station is shown in Figure 1a.
155 Additional quality control measures were applied to ensure the reliability of the hourly
156 observations used in developing the IDF curves. Stations were ~~included~~~~considered~~ if they had
157 less than 10% missing data per year. Besides, to ensure a robust sample size for fitting the GEV
158 distribution, only stations with at least 10 years of precipitation records were retained (Ren et al.,
159 2025). Consequently, the data record for the selected stations span from 1951 to 2020, with
160 record lengths ranging from 10 to 70 years, as shown in Figure 1b. To address missing data and
161 prevent underestimation, gaps were handled as follows: (1) for ~~continuous~~-missing periods less
162 than 12 hours, ~~the~~ the recorded hourly data were~~precipitation recorded hourly was~~ linearly
163 interpolated; (2) for continuous gaps of 12 hours or ~~longer~~~~more~~, no interpolation was
164 ~~attempted~~~~performed~~, and the hours with missing ~~data~~~~hours~~ were ~~directly~~-assigned a value of
165 zero. From these quality-controlled hourly observations, 27 extreme hourly indices were
166 extracted. Specifically, the annual maximum rainfall for durations from 1 to 24 hours by 1-hour
167 increments, as well as longer durations of 36-hour, 48-hour, and 72-hour-~~durations~~, were
168 identified on a yearly basis using a moving window method, resulting in an annual maximum
169 series for each location.

170 The CHM_PRE dataset is a high-quality gridded precipitation dataset covering mainland
171 China. The daily dataset spans the period from 1961 to 2022, with multiple spatial resolutions
172 ($0.1^\circ \times 0.1^\circ$, $0.25^\circ \times 0.25^\circ$, and $0.5^\circ \times 0.5^\circ$)~~and a daily temporal resolution~~. It is constructed using
173 daily observations from 2839 gauges across China and nearby regions, employing an
174 interpolation scheme that combines the Parameter-elevation Regression on Independent Slopes
175 Model (PRISM) for the daily climatology field with inverse-distance weighting to interpolate
176 station observations into the ratio field (Han et al., 2023). In this study, $0.1^\circ \times 0.1^\circ$ CHM_PRE was
177 selected. CHM_PRE served as the primary independent variable for the machine learning
178 methods, providing essential input for regionalizing IDF curves across mainland China. Since the
179 dependent variable was based on hourly observations, utilizing independent variables derived
180 from such daily observations did not pose a risk of data leakage. In addition to CHM_PRE, we also
181 explored the CGDPP (Shen et al., 2010) and CHIRPS (Funk et al., 2015) datasets (Tables S1 to S12).
182 However, since they did not demonstrate better performance compared to CHM_PRE, they were
183 not selected for this study.



184
185 **Figure 1.** The spatial distribution of 2363 stations with hourly observations-records used for in
186 this study, showing (a) the number of operational months per year, and (b) record lengths. The
187 inset displays the South China Sea Islands within the nine-dash line. The spatial distribution of
188 2363 hourly observation records used in this study showing (a) The number of operational
189 months per year, and (b) record lengths.

190 2.2 Development of IDF curves

191 The construction of Intensity-Duration-Frequency (IDF) curves in this study follows the
192 Koutsoyiannis method, which calculates generalized rainfall intensity as a function of duration
193 (Koutsoyiannis et al., 1998). Specifically, the generalized intensity i is formulated as:

$$194 \quad i = i_d \cdot b_d \quad (1)$$

195 Here, d denotes the duration in hours, and i_d is the intensity calculated by using the annual
196 maximum series (AMS) method for each duration. The function b_d is:

$$197 \quad b_d = (d + \theta)^\eta \quad (2)$$

198 where the parameters θ and η are estimated for each station by minimizing the Kruskal–Wallis
199 statistic (Koutsoyiannis et al., 1998). Having estimated After determining θ and η , the generalized
200 intensities i for all duration levels are pooled together under the assumption that they follow the
201 same distribution for all durations. For the distribution fitting process, this study employs the
202 Generalized Extreme Value (GEV) distribution. The GEV distribution function (Jenkinson, 1955)
203 can be expressed as:

$$204 \quad G(z; \mu, \sigma, \xi) = \exp \left\{ - \left[1 + \xi \left(\frac{z - \mu}{\sigma} \right) \right]^{-1/\xi} \right\}, 1 + \frac{\xi(z - \mu)}{\sigma} > 0, \xi \neq 0 \quad (3)$$

205 where μ is the location parameter, σ is the scale parameter, and ξ is the shape parameter. These
206 parameters can be estimated with by using the L-moment method (Hosking, 1990). Once the GEV
207 parameters were determined, the corresponding $(1 - r^{-1})$ -th quantile of the GEV distribution
208 for a r -year return period could be calculated. The IDF curves are finally generated by estimating
209 quantiles at specific return periods from the fitted GEV distribution and dividing these quantiles
210 by the term b_d . In this study, the durations selected were each-whole hours from 1 to 24, along
211 with 36, 48, and 72 hours, and the return periods were 2, 5, 10, 20, 50, 100, 200, 500, and 1000
212 years.

213 2.3 The spatial interpolation methods

214 Traditional spatial interpolation methods were used in this study to regionalize IDF curves.
215 Both deterministic interpolation and geostatistical interpolation methods were utilized. Inverse
216 Distance Weighted (IDW) represents a deterministic interpolation method, while ~~K~~riging is a
217 form of geostatistical interpolation.

218 The fundamental principle of IDW is that the influence of a known point diminishes with
219 increasing distance from the unknown point. Mathematically, the estimated value $\hat{Z}(x_0)$ at
220 location x_0 is calculated as follows:

221
$$\hat{Z}(x_0) = \frac{\sum_{i=1}^n \frac{Z(x_i)}{d(x_i, x_0)^p}}{\sum_{i=1}^n \frac{1}{d(x_i, x_0)^p}} \quad (4)$$

222 where $Z(x_i)$ represents the known value at location x_i , $d(x_i, x_0)$ is the Euclidian distance
223 between the known point x_i and the unknown point x_0 , p is the power parameter that controls
224 the rate of decay of influence with distance, and n is the number of known points used in the
225 interpolation. In this study, the IDW method was implemented using a power parameter p of 2,
226 which is a commonly used value that provides a balance between smoothness and accuracy (Li
227 & Heap, 2008).

228 Kriging interpolation is a geostatistical method that assumes a stochastic process with
229 spatial correlation between different points. The core of Kriging interpolation lies in the
230 calculation of the variogram, which represents the spatial correlation between points at different
231 distances. Initially, various lag distances are defined, and the semi-variance of residuals at these
232 lag distances is calculated to generate the ~~empirical~~~~experimental~~ variogram. The formula for the
233 semi-variance (Armstrong, 1998) is as follows:

234
$$\gamma(h) = \frac{1}{2N(h)} \sum_{i=1}^{N(h)} [Z(x_i) - Z(x_i + h)]^2 \quad (5)$$

235 where $\gamma(h)$ is the semivariance at lag distance h , $N(h)$ is the number of pairs of points separated
236 by h , $Z(x_i)$ is the value at location x_i , and $Z(x_i + h)$ is the value at location $x_i + h$. Subsequently,
237 a theoretical model is fitted to the ~~empirical~~~~experimental~~ variogram. In this study, the commonly
238 used spherical model was employed.

239 Ordinary Kriging (OK) assumes that the trend is an unknown constant. The formula
240 (Verworn & Haberlandt, 2011) for Ordinary Kriging is:

241
$$\hat{Z}(x_0) = \sum_{i=1}^n \lambda_i Z(x_i) \quad (6)$$

242 where $\hat{Z}(x_0)$ is the estimated value at location x_0 , λ_i are the weights, and $Z(x_i)$ are the known
243 values at locations x_i . The weights are determined using the Kriging equations based on the
244 variogram.

245 Kriging with External Drift (KED) incorporates one or more auxiliary variables as
246 background information for the interpolation of the primary variable. KED assumes that the
247 expectation of the primary variable is a linear combination of these auxiliary variables (Verworn
248 & Haberlandt, 2011):

249
$$E[Z(x) | Y_1(x), Y_2(x), \dots, Y_m(x)] = \beta_0 + \sum_{k=1}^m \beta_k Y_k(x) \quad (7)$$

250 where $E[Z(x) | Y_1(x), Y_2(x), \dots, Y_m(x)]$ is the expectation of the primary variable at location x ,
251 $\beta_0, \beta_1, \dots, \beta_m$ are the unknown constants, and $Y_1(x), Y_2(x), \dots, Y_m(x)$ are the auxiliary
252 variables. It is important to note that when calculating the variogram using the KED method,
253 $E[Z(x) | Y_1(x), Y_2(x), \dots, Y_m(x)]$ at different spatial points vary. Therefore, the residuals must
254 be calculated first, and then the semi-variance based on residuals is computed. The residuals are
255 calculated as: $R(x) = Z(x) - E[Z(x)]$. In this study, annual precipitation and elevation were
256 used as auxiliary variables (Table 1). The spatial resolution of the annual precipitation data and
257 the elevation data were both $1\text{km} \times 1\text{km}$. The interpolation methods were all performed using
258 the 'gstat' package in R (Pebesma, 2004).

259 2.4 Machine learning methods

260 In this study, machine learning methods were applied using the scikit-learn (sklearn)
261 library in Python (Pedregosa et al., 2011), taking advantage of the CHM_PRE dataset (see Section
262 2.1). For each grid cell, we first calculated a set of independent variables, grouped into four
263 categories: geographic coordinates and elevation, statistics of annual and daily precipitation
264 statistical features, and daily extreme precipitation for different return periods (Table 1). These
265 selected and readily available independent variables without introducing additional other
266 meteorological variables allow for testing the predictive potential inherent within the
267 precipitation data, while also ensuring the method's practicality and applicability, particularly in
268 regions where other high-quality meteorological data are limited or unavailable. We then aligned
269 each observational station to the grid cell in which the station is located, and treated the station-
270 derived rainfall intensity at specific duration and frequency as dependent target variables. The
271 datasets used to evaluate prediction accuracy were based on all grids that contained both
272 independent and dependent variables.

273

274
275
276

Table 1. Independent variables used in the regionalization methods evaluated. The gridded precipitation data are sourced from CHM_PRE.

Regionalization methods	Category	Description
<i>site-observation-based interpolation method</i>	1. geographic coordinates	latitude longitude
	2. primary variables	Rainfall intensities for 27 durations and 9 return periods based on hourly observations (see Section 2.2)
	3. auxiliary variables	The elevation derived from 1km grid (Figure S1) The mean annual precipitation derived from CHM_PRE (Figure S2)
<i>gridded-precipitation-based machine learning method</i>	1. geographic coordinates and elevation	latitude of the centre of each grid cell longitude of the centre of each grid cell The elevation derived from 1km grid (Figure S1)
	2. annual precipitation statistical features	The mean annual precipitation The standard deviation of annual precipitation The skewness of annual precipitation derived The kurtosis of annual precipitation derived
	3. daily precipitation statistical features	The mean daily precipitation The standard deviation of daily precipitation The skewness of daily precipitation The kurtosis of daily precipitation

The mean annual maximum daily precipitation

The mean annual 95th percentile daily precipitation

The average of the annual sums of daily precipitation that exceeds 95th percentile of daily precipitation for the year

4. daily extreme precipitation

Daily precipitation for 9 return periods (2, 5, 10, 20, 50, 100, 200, 500, and 1000 years). Note that the daily duration is not equivalent to the 24-hour duration, as the latter is based on the moving window method.

277

278 Then a range of four general test cases were extracted from the IDF curves that, for
279 simplicity, are referred to herein as the short duration-small return period (SDSR), short duration-
280 large return period (SDLR), long duration-small return period (LDSR), and long duration-large
281 return period (LDLR) cases, corresponding to the four permutations of IDF cases with 1-hr and
282 24-hr durations, and 5-yr and 100-yr return periods. These targets were selected to represent
283 varying durations and return periods, thereby capturing the different scales of extremes within
284 the IDF framework. These selected cases were used to evaluate the performance of the different
285 regionalization methods.

286 To predict extreme rainfall intensities, 10 different machine learning methods (Table S13)
287 were considered initially, and cross-validation was used to evaluate their accuracy. For each case,
288 we calculated performance scores according to the procedure described in Section 2.5. The five
289 highest-scoring machine learning methods, based on the average scores across all the four cases,
290 were Random Forest (RF), Gradient Boosting (GB), Extremely Randomized Trees (ET), Multilayer
291 Perceptron (MLP), and Linear Regression (LR) (Breiman, 2001; Friedman, 2001; Geurts et al., 2006;
292 Hinton, 1989).

293 It should be noted that we also performed hyperparameter tuning using a grid search for
294 each model ~~for~~ the four cases (Tables S14 to S17). However, the best performance among all
295 machine learning methods with tuned hyperparameters did not show a significant improvement
296 over that with the default settings provided by the Scikit-learn library. [Additional experiments
297 using Bayesian optimization \(Mockus, 1998; Snoek et al., 2012\) to search for optimal
298 hyperparameters also failed to yield notable improvement \(Tables S18 to S22\).](#) Consequently, for
299 simplicity and consistency, we proceeded with the default hyperparameters throughout the
300 study.

301 2.5 Evaluation of the regionalization efficiency

302 This study employed five-fold cross-validation to evaluate the prediction accuracy of
303 interpolation and machine learning methods. Additionally, cross-validation helps mitigate the
304 risk of overfitting, ensuring more robust and generalizable results. In each iteration, 80% of the

305 data was used to train the model, while the remaining 20% was reserved for validation. This
 306 process was repeated five times using sampling without replacement, ensuring that each data
 307 point was used for validation exactly once.~~This process was repeated five times, ensuring each~~
 308 ~~data point was included in both the training and prediction phases.~~ The predicted values were
 309 then compared with the observations to evaluate accuracy using the following metrics: Nash-
 310 Sutcliffe Efficiency (NSE), Percent Bias (PBIAS), Root Mean Square Error (RMSE), and Kling-Gupta
 311 Efficiency (KGE). The formulas for these evaluation metrics are provided below:

$$312 \quad NSE = 1 - \frac{\sum_{i=1}^n (O_i - P_i)^2}{\sum_{i=1}^n (O_i - \bar{O})^2} \quad (8)$$

$$313 \quad PBIAS = 100\% \times \frac{\sum_{i=1}^n (P_i - O_i)}{\sum_{i=1}^n O_i} \quad (9)$$

$$314 \quad RMSE = \sqrt{\frac{\sum_{i=1}^n (P_i - O_i)^2}{n}} \quad (10)$$

$$315 \quad KGE = 1 - \sqrt{(CC - 1)^2 + \left(\frac{\sigma_P}{\sigma_O} - 1\right)^2 + \left(\frac{\bar{P}}{\bar{O}} - 1\right)^2} \quad (11)$$

316 where O_i denotes the observed values, P_i denotes the predicted values. Specifically, O_i is the
 317 extreme rainfall intensity for a given duration and return period estimated from hourly data at
 318 an individual site, while P_i is the corresponding value for that site predicted by a model (either
 319 interpolation or machine learning) trained on data that excluded the site being evaluated. \bar{O} and
 320 \bar{P} are the mean of the observed and the predicted values, respectively. σ_O and σ_P are the
 321 standard deviations of the observed and predicted values, respectively. CC is the Pearson
 322 correlation coefficient:

$$323 \quad CC = \frac{\sum_{i=1}^n (P_i - \bar{P})(O_i - \bar{O})}{\sqrt{\sum_{i=1}^n (P_i - \bar{P})^2} \sqrt{\sum_{i=1}^n (O_i - \bar{O})^2}} \quad (12)$$

324 The maximum value for NSE is 1, with higher values indicating better predictive
 325 performance. PBIAS values indicate overestimation (positive) or underestimation (negative), with
 326 lower absolute values representing smaller prediction errors. RMSE has a minimum value of 0,
 327 where smaller values denote less error. KGE reflects the correlation, variability, and bias between
 328 predicted and observed values, with its maximum value being 1 and higher values indicating
 329 better performance.

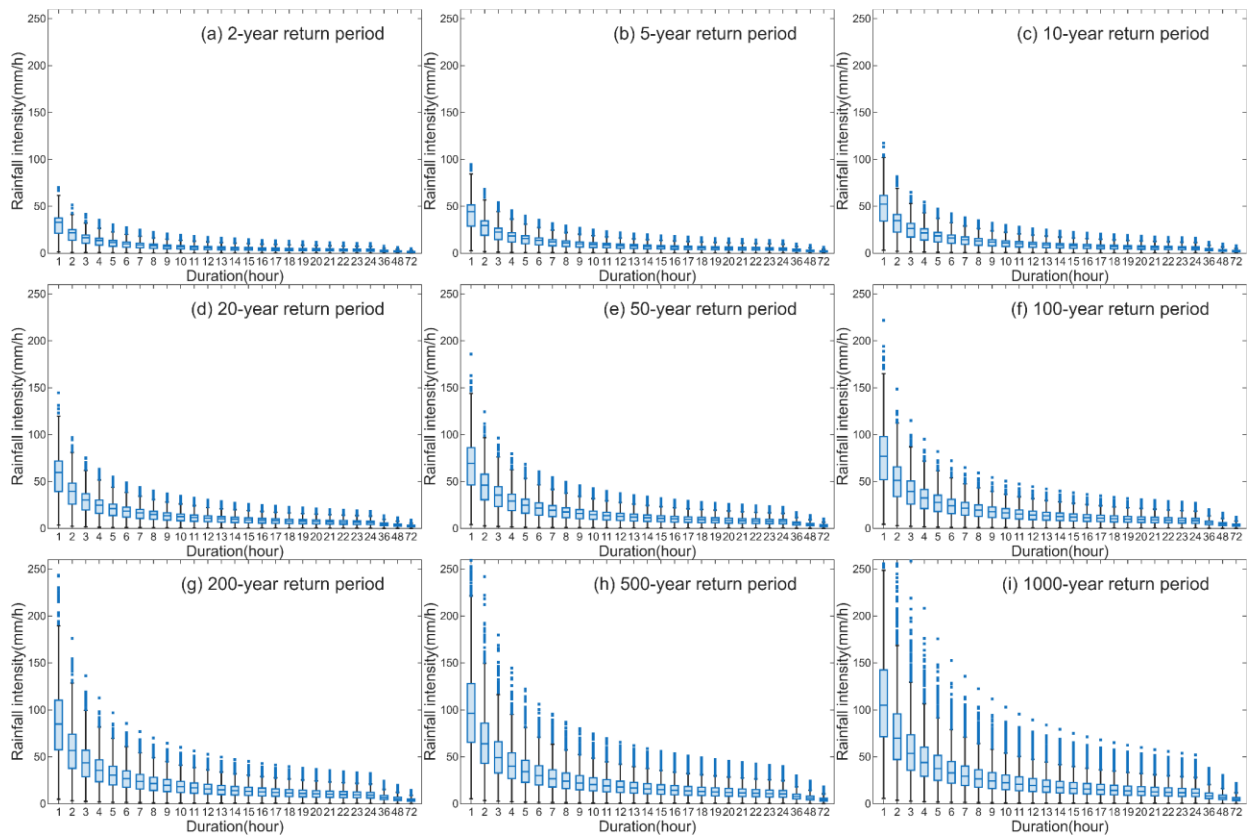
330 To determine the optimal regionalization method for each specific duration and return
 331 period ~~extreme~~, a weighted composite score based on the above four metrics was defined. First,
 332 each metric was individually standardized using standard deviation normalization among all
 333 methods (mean of 0, with positive or negative values indicating above or below the mean,
 334 respectively, and the values representing multiples of the standard deviation from the mean).
 335 The standardized metrics were then weighted and averaged to calculate the final score for each
 336 method using assigned weights of 0.2, 0.2, 0.2, and 0.4, respectively (RMSE's standardized values
 337 were negated, and PBIAS values were first converted to absolute values before negation). The
 338 method with the highest weighted composite score was selected as the optimal regionalization
 339 method for the given duration and return period. This selection process was performed for the
 340 permutations of 27 durations and 9 return periods ($27 \times 9 = 243$ times). The selected optimal

341 regionalization method was then applied to regionalize extreme rainfall intensity for each specific
342 duration and return period.

343 3 Results

344 3.1 Station-level IDF curves in Mainland China

345 To establish a foundation for regionalizing IDF curves ~~regionalization~~, we first analyzed
346 station-level IDF curves derived from the observed rainfall data across the NMIC ground network.
347 These station-specific IDF curves, serving as the dependent variable in subsequent analyses,
348 provide the most precise-accurate representation of extreme rainfall intensities (Figure 2). The
349 specific statistical characteristics of the four IDF cases used to test regionalization methods are
350 summarized in Table [S2&S49](#). The mean values clearly highlight differences in the magnitude of
351 rainfall intensity across the cases. The LDSR exhibits a mean intensity of 4.5 mm/h, whereas the
352 LDLR shows a significantly higher mean intensity of 8.42 mm/h, indicating higher rainfall intensity.
353 This pattern of increasing rainfall intensity with larger return periods is evident for both short and
354 long durations. In addition, the mean intensity for shorter durations, such as the SDLR (76.38
355 mm/h), is much higher compared to longer durations like the LDLR. These results emphasize the
356 variations in IDF curves: shorter durations and larger return periods correspond to higher rainfall
357 intensities, underscoring the increasing severity, which can also be inferred to in Section 2.2. Such
358 rainfall intensity of shorter durations and larger return periods may pose additional challenges
359 for accurate prediction.



360

361 **Figure 2.** Boxplots of observed station-level rainfall intensities for various durations and return
 362 periods across stations in mainland China.

363 3.2 Evaluation of regionalization method types

364 To evaluate the performance and reliability of different methods for regionalizing IDF
 365 curves across mainland China, this study systematically compares five traditional interpolation
 366 methods and five machine learning methods. The objective is to assess the predictive capabilities
 367 of these methods, explore the potential of machine learning methods for regionalizing IDF curves,
 368 and demonstrate the reliability of the regionalized IDF curves product created by applying the
 369 optimal method (selected from the ten evaluated methods) to each of the four IDF cases with a
 370 specific duration and return period combination.

371 3.2.1 Interpolation methods

372 Prediction accuracy for the five interpolation methods and five machine learning methods
 373 across four cases are presented in Table 2 and Table 3, respectively. The weighted composite
 374 scores derived from these metrics are shown in Figure 3. Among the interpolation methods,
 375 Inverse Distance Weighting (IDW), a deterministic interpolation technique, consistently
 376 underperformed compared to the geostatistical models represented by the Kriging methods
 377 (Figure 3). This performance gap was particularly evident for ~~the~~ cases with smaller return
 378 periods. As shown in Table 2, IDW exhibited inferior performance relative to the Kriging methods
 379 across almost all performance metrics for ~~the~~ cases with smaller return periods.

380 Among the four Kriging methods, Kriging with External Drift using annual average
 381 precipitation (KED_AP) demonstrated improved scores across all four cases compared to
 382 Ordinary Kriging (OK) which does not incorporate covariates (Figure 3). However, when elevation
 383 was used as a covariate (KED_DEM), scores declined ~~for~~ all ~~of~~ the four cases. Similarly, when
 384 both annual precipitation and elevation were included as covariates (KED_DEM+AP), the pattern
 385 remained consistent with KED_DEM, showing decreased scores ~~for~~ all ~~of~~ the four cases
 386 compared to KED_AP (Figure 3). These trends were further corroborated in terms of ~~by the~~
 387 ~~metrics of~~ NSE, PBIAS, RMSE, and KGE presented in Table 2, which are largely aligned ed with the
 388 observed score patterns.

389 **Table 2.** Accuracy metrics of interpolation methods in mainland China.

	SDSR				SDLR				LDSR				LDLR			
	NSE	PBIAS	RMSE	KGE	NSE	PBIAS	RMSE	KGE	NSE	PBIAS	RMSE	KGE	NSE	PBIAS	RMSE	KGE
IDW	0.93	0.70%	4.22	0.92	0.78	0.71%	15.06	0.82	0.91	0.28%	0.57	0.91	0.81	0.43%	1.69	0.83
OK	0.94	-0.06%	3.92	0.95	0.79	0.06%	14.92	0.82	0.93	-0.01%	0.50	0.94	0.81	0.11%	1.69	0.84
KED_AP	0.94	0.03%	3.79	0.96	0.79	-0.01%	14.72	0.84	0.95	0.07%	0.45	0.96	0.82	0.05%	1.60	0.87
KED_DEM	0.93	0.21%	4.06	0.94	0.78	0.33%	15.24	0.83	0.92	0.07%	0.56	0.93	0.78	0.24%	1.80	0.83
KED_DEM+AP	0.94	0.12%	3.77	0.96	0.79	0.16%	14.89	0.85	0.94	0.12%	0.46	0.96	0.82	0.11%	1.64	0.87

*NSE and KGE are dimensionless and, RMSE is in mm/h, and PBIAS is in percentage (%).
Positive (Negative) PBIAS (in percentage) indicates overestimation (underestimation).

These results indicate that IDW is less effective at predicting extreme rainfall intensities compared to Kriging methods across the four cases. Among the Kriging methods, incorporating annual precipitation as a covariate significantly improved prediction accuracy, whereas including elevation as a covariate did not, and in some cases, even with reduced accuracy. This finding is consistent with previous studies conducted in the Haihe River Basin, China (Zou et al., 2021).

3.2.2 Machine learning methods

As shown in Figure 3, among the five machine learning methods, Gradient Boosting (GB) performed the best, achieving the highest scores for all cases. In the final regionalized IDF curves, GB also outperformed the other methods and became the optimal method in many cases (Table S18S31). Following GB’s performance, both Random Forest (RF) and Extremely Randomized Trees (ET) demonstrated relatively stable performance across the four cases, showing acceptable scores with relatively small variability. In contrast, MLP and Linear Regression (LR) exhibited greater performance variability across the four cases (Figure 3). For instance, while MLP achieved high scores for longer durations, its accuracy for shorter durations was notably lower, as indicated by the lower NSE and higher RMSE and PBIAS values (Table 3). However, the strength of MLP’s accuracy in longer-duration cases allowed it to surpass GB and become the optimal method in certain longer-duration cases within the final regionalized IDF curves (Table S18S31).

Table 3. Accuracy metrics of machine learning methods in mainland China.

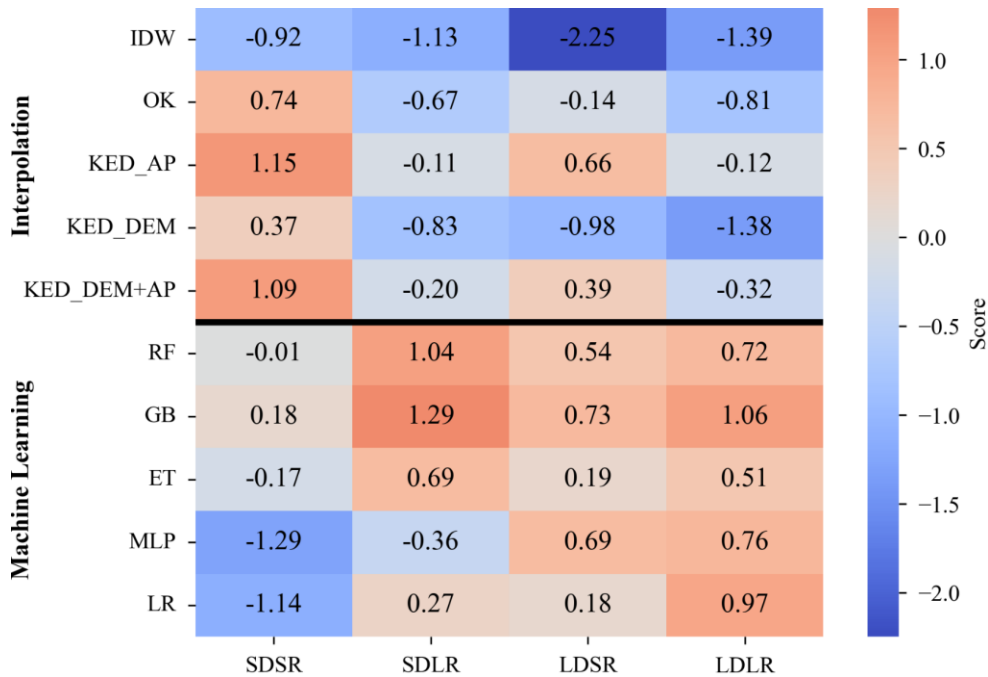
	SDSR				SDLR				LDSR				LDLR			
	NSE	PBIAS	RMSE	KGE	NSE	PBIAS	RMSE	KGE	NSE	PBIAS	RMSE	KGE	NSE	PBIAS	RMSE	KGE
RF	0.92	0.16%	4.34	0.94	0.83	0.37%	13.49	0.87	0.94	-0.03%	0.47	0.96	0.87	0.22%	1.37	0.91
GB	0.92	-0.02%	4.34	0.94	0.83	0.11%	13.29	0.87	0.95	-0.07%	0.44	0.96	0.88	-0.05%	1.36	0.91
ET	0.92	0.10%	4.50	0.93	0.82	0.41%	13.93	0.87	0.93	0.01%	0.50	0.95	0.86	0.18%	1.45	0.90
MLP	0.88	-0.50%	5.36	0.93	0.78	-1.21%	15.10	0.87	0.95	-0.14%	0.45	0.97	0.87	0.18%	1.37	0.91
LR	0.89	0.00%	5.24	0.92	0.80	0.05%	14.56	0.86	0.93	-0.04%	0.50	0.95	0.87	0.00%	1.41	0.91

*NSE and KGE are dimensionless and RMSE is in mm/h. Positive (Negative) PBIAS (in percentage) indicates overestimation (underestimation).

*NSE and KGE are dimensionless, RMSE is in mm/h, and PBIAS is in percentage (%).

417 3.2.3 Comparison between interpolation and machine learning methods

418 When comparing interpolation and machine learning methods, the highest composite
 419 scores for SDSR, SDLR, LDSR, and LDLR were achieved with KED_AP, GB, GB, and GB, respectively
 420 (Figure 3). Notably, the difference in relative scores between the best interpolation and machine
 421 learning methods indicate that the performance gap narrows—and may even reverse—as the
 422 duration and return period increase (e.g., the score difference is 0.97 for SDSR and -1.18 for LDLR).
 423 This trend indicates that machine learning methods tend to perform ~~relatively~~ better as the
 424 duration and return period increase. This observation is further supported by the final IDF curves
 425 dataset (Table 518531). Furthermore, as shown in Table 2 and Table 3, the initial hypothesis in
 426 Section 3.1 is confirmed: shorter duration and larger return periods are usually associated with
 427 increased prediction difficulty and reduced accuracy.



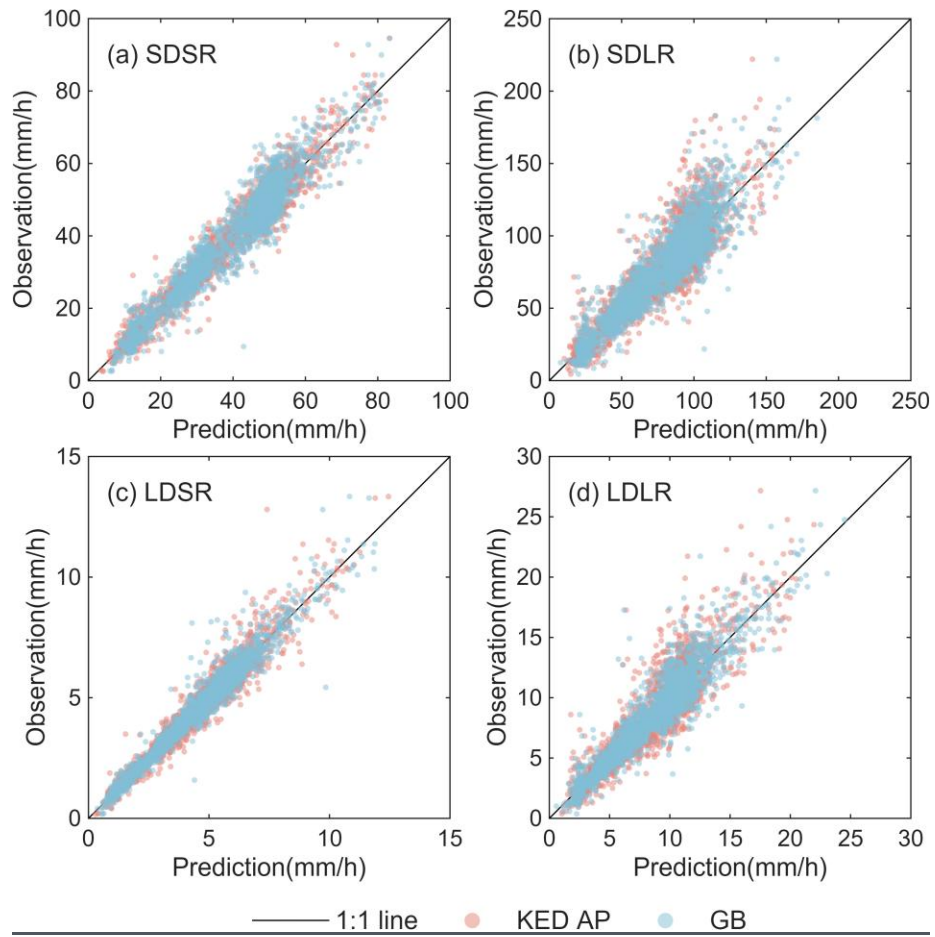
428 **Figure 3.** Weighted composite scores of all regionalization methods. Larger, more positive
 429 values represent better performance, with a value of 0 representing average performance.
 430

431
 432 Methods with the highest scores from both interpolation and machine learning methods
 433 demonstrated strong performance across the four cases. For the most challenging case, SDLR,
 434 the highest scoring methods—KED_AP from the interpolation techniques and GB from the
 435 machine learning models—achieved KGE values not less than 0.84. For SDSR, LDSR, and LDLR, the
 436 highest scoring methods from both interpolation and machine learning methods produced KGE
 437 values of at least 0.94, 0.96, and 0.87, respectively, with PBIAS values close to zero, indicating
 438 little systematic bias (Table 2 and Table 3).

439 In the subsequent sections, this study focuses on KED_AP and GB, which consistently
 440 demonstrated strong and stable performance across the four cases, as representative examples
 441 of interpolation and machine learning methods, respectively. These two methods are used to
 442 ~~display-show~~ the predictive results at various stations, highlighting both the potential of

443 interpolation and machine learning methods for IDF regionalization and the regional variations
444 in performance.

445 Figure 4 presents the prediction results from both interpolation and machine learning.
446 For all four cases, estimated extreme rainfall intensities are generally aligned along the 1:1 line.
447 In terms of distribution, the scatter points for the two cases with smaller return periods are more
448 closely concentrated around the 1:1 line, while those for larger return periods exhibit greater
449 dispersion (Figure 4). In addition, analysis of relative errors (Figure S53) reveals comparable
450 performance between the two methods across all cases. The relative errors are notably smaller
451 for smaller return periods (median RE: 0.39-0.65%) compared to larger return periods (median
452 RE: 1.5-2.5%), indicating increased prediction uncertainty for more extreme events.



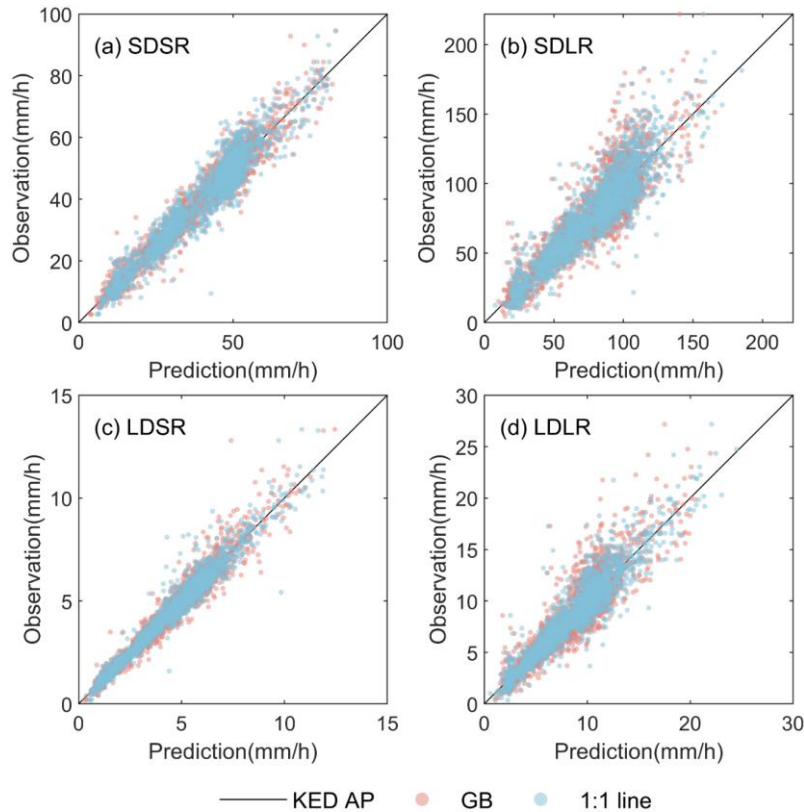
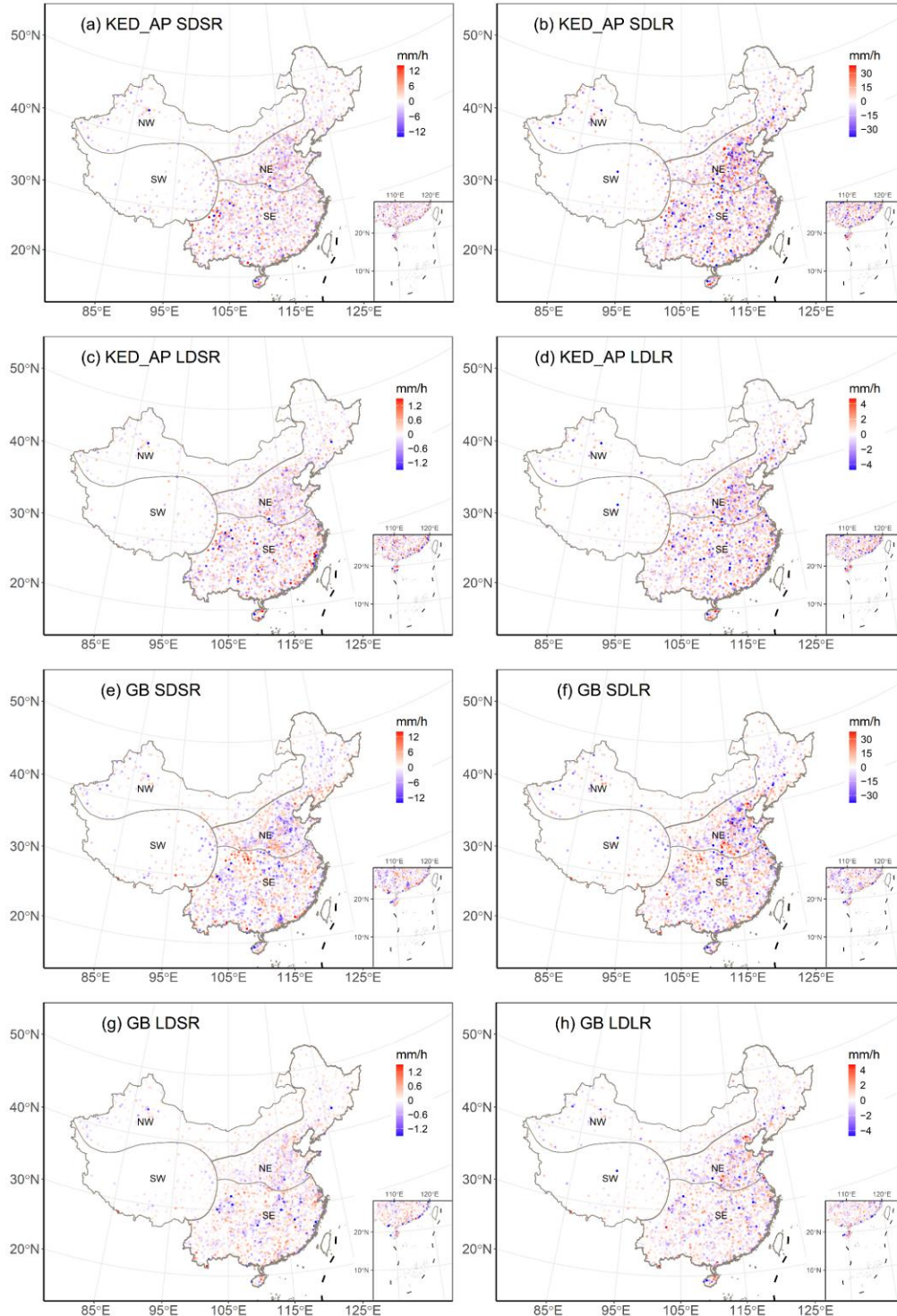


Figure 4. Scatterplots of observations and predictions for KED_AP (the best interpolation method) and GB (the best machine learning method).

The residuals (calculated as the difference between predicted and observed values) for both methods mostly show distributions that are close to be normally distributed (Figure S64). However, compared to ~~a~~the true normal distribution, the residual distributions still exhibit mild negative skewness and higher kurtosis, suggesting that both methods tend to underestimate certain extreme values. These underestimation is evident in Figure 4, where the corresponding values are scattered above the 1:1 line. For an ideal model, the residuals should be randomly distributed across the study area, with no obvious spatial patterns influenced by location or the magnitude of observed values. The spatial distribution of residuals is illustrated in Figure 5. The overall spatial distribution of residuals is relatively random, with no obvious clustering or trend. Consistent with the findings from Figure S64, there are marginally more instances of severe underestimation than severe overestimation across all cases. The above results of residual analysis also indicate that the predictive performance of interpolation and machine learning is satisfactory, with both providing reliable predictions across mainland China.



470
 471 **Figure 5.** Spatial distribution of the residuals for KED_AP (the best interpolation method, (a)-(d))
 472 and GB (the best machine learning method, (e)-(h)). Blue points represent underestimation,
 473 while red points represent overestimation.

474 In short, ~~when comparing both~~ interpolation and machine learning methods, ~~both~~
 475 ~~methods~~ demonstrate comparable and robust performance across various cases, whether for

476 short or long durations and return periods. This consistent accuracy in terms of accuracy metrics,
477 residuals, and relative errors highlights the strong potential of ~~the two~~ ~~both~~ methods for the
478 regionalization of IDF curves in mainland China. Notably, machine learning, as a method not
479 previously applied to IDF curves regionalization in mainland China, demonstrates accuracy
480 comparable to traditional interpolation methods and even outperforms them in predicting cases
481 for long durations and large return periods. Additionally, machine learning offers distinct
482 advantages, such as requiring only daily precipitation data ~~in order to perform for~~ regionalization
483 once a model is trained (in contrast with interpolation methods, which always require known
484 sub-daily level target values). Furthermore, machine learning is independent of station setup
485 conditions, and possesses strong adaptability for future updates, forecasting, and climate
486 projection. These features suggest that machine learning has the potential to replace
487 interpolation methods in future IDF curves regionalization applications.

488 3.3 Regional performance evaluation of interpolation and machine learning methods

489 A method that performs well at the national level may exhibit poor accuracy for specific
490 regions. To address this, this study adopted a regionalization scheme that divides mainland China
491 into four regions (See Section 2.1). Using this scheme, we conducted a regional assessment across
492 mainland China, using KED_AP and GB as representatives of interpolation and machine learning
493 methods, respectively, to explore their applicability in the four distinct regions. Notably, we did
494 not retrain the models for regional scales but used the nationally trained models to compute
495 accuracy metrics within each region.

496 As an interpolation method, the predictive accuracy of KED_AP is influenced by station
497 density and whether the interpolation assumptions, ~~—~~ such as decreasing correlation with
498 distance, ~~—~~ are satisfied. In the NE region, where station density is high and precipitation patterns
499 are relatively stable, KED_AP achieves high predictive accuracy, with a KGE of 0.94 for SDSR and
500 LDSR (Table 4). In contrast, in the SE region, characterized by a humid subtropical and monsoon
501 climate, the performance of KED_AP declines for SDSR, SDLR, and LDSR compared to the NE
502 region, despite the dense station network (Table 4). This decline is likely due to the more extreme
503 nature of precipitation in the SE region, which may gradually violate the assumption of decreasing
504 correlation with distance. In the NW region, precipitation extremes are less pronounced due to
505 its inland location, but the low station density reduces predictive accuracy compared to the NE
506 region (Table 4). Lastly, in the SW region, KED_AP performs significantly worse across all four IDF
507 cases, with the highest KGE for LDSR reaching only 0.72 (Table 4). As shown in Figure S1, the
508 poor accuracy in the SW region may be attributed to the sparse station density and the region's
509 complex topography, which greatly affects interpolation accuracy, consistent with findings in
510 previous studies (Miao et al., 2024).

511 The machine learning method, GB, demonstrates notable adaptability across most
512 regions and is often comparable to or better than interpolation methods, particularly for longer
513 durations and return periods. As shown in Table 4, in the NE region, GB achieves a KGE of 0.92
514 for SDSR, closely matching KED_AP's performance of 0.94. For LDSR, GB's KGE reaches 0.95,
515 slightly exceeding that of KED_AP. In the SE region, although GB slightly underperforms KED_AP
516 for shorter durations and return periods (e.g., KGE of 0.86 for SDSR compared to 0.88 for KED_AP),
517 its relative performance improves as duration and return period increase. For example, for LDLR,

518 GB achieves a KGE of 0.87, surpassing KED_AP's KGE of 0.79. Similarly, in the NW region, GB's
 519 performance for LDLR reaches a KGE of 0.77, exceeding KED_AP's KGE of 0.68. However, in the
 520 SW region, GB's performance is considerably lower than that in other regions across all four IDF
 521 cases, with the highest KGE reaching only 0.65. This underperformance is likely attributable to
 522 the pronounced terrain undulation and sparse station distribution in the SW region, where the
 523 complex precipitation patterns are challenging for a nationally trained GB model to capture
 524 accurately. Additionally, the representativeness errors in the gridded precipitation data may
 525 further hinder the accuracy of the machine learning method in this region. Overall, the results
 526 demonstrate that GB exhibits notable adaptability across most regions, with its predictive
 527 accuracy relative to interpolation methods improving as duration and return periods increase,
 528 thereby demonstrating the robustness of this trend at the national level.

529

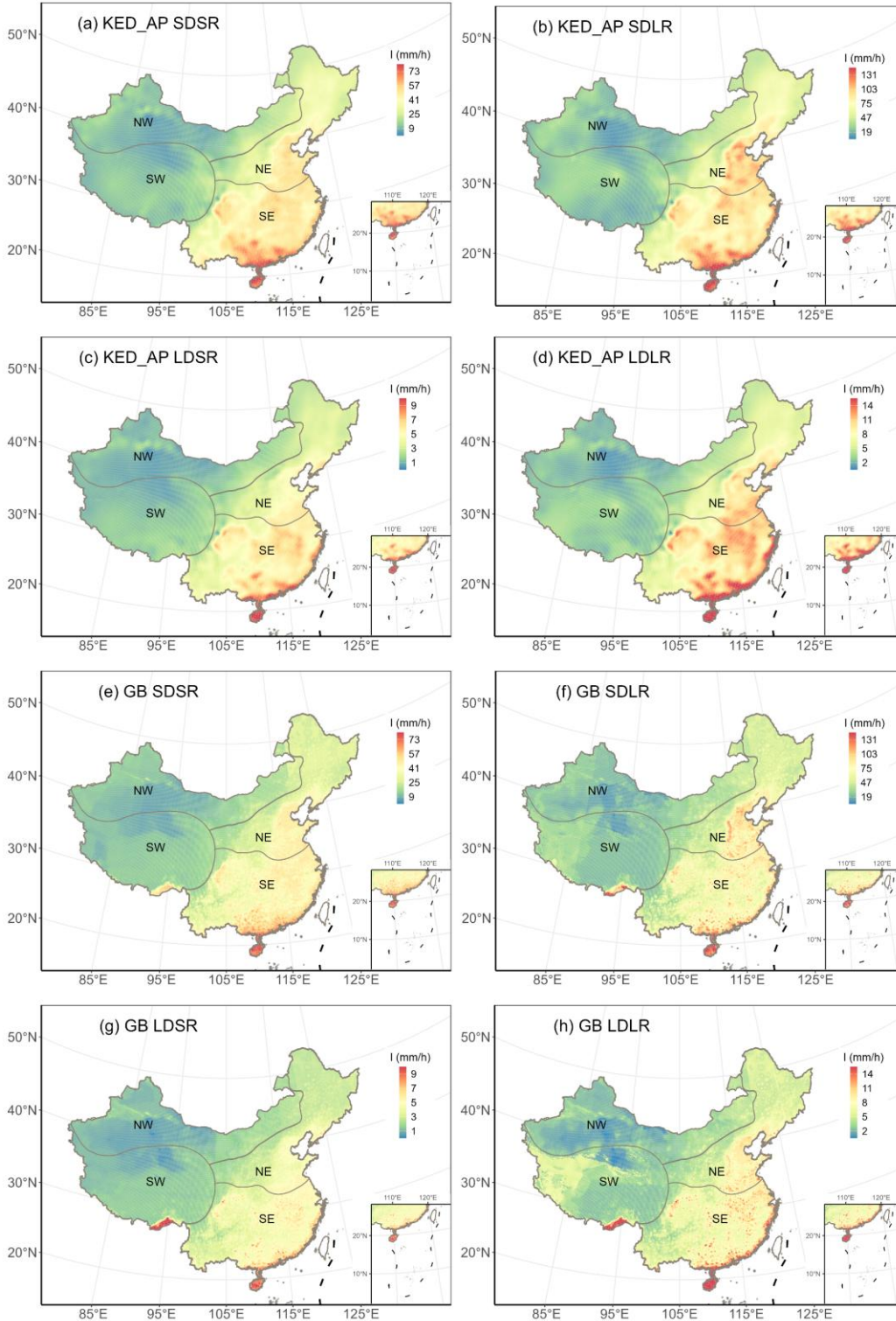
530 **Table 4.** Regional accuracy metrics for KED_AP (the best interpolation method) and GB
 531 (the best machine learning method).

	SDSR				SDLR				LDSR				LDLR			
	<i>NSE</i>	<i>PBIAS</i>	<i>RMSE</i>	<i>KGE</i>	<i>NSE</i>	<i>PBIAS</i>	<i>RMSE</i>	<i>KGE</i>	<i>NSE</i>	<i>PBIAS</i>	<i>RMSE</i>	<i>KGE</i>	<i>NSE</i>	<i>PBIAS</i>	<i>RMSE</i>	<i>KGE</i>
<i>The interpolation method: Kriging methods incorporating annual precipitation as a covariate (KED_AP)</i>																
NE	0.92	-0.10	3.32	0.94	0.73	-0.06	15.12	0.78	0.92	-0.11	0.32	0.94	0.71	-0.32	1.54	0.77
NW	0.79	-0.50	2.98	0.87	0.47	-0.74	10.46	0.63	0.86	0.07	0.26	0.90	0.55	-0.79	0.98	0.68
SW	0.46	0.06	3.05	0.65	0.13	0.55	9.47	0.31	0.52	0.81	0.25	0.72	-0.12	2.84	1.10	0.03
SE	0.85	0.14	4.30	0.88	0.65	0.05	15.46	0.72	0.88	0.15	0.56	0.91	0.74	0.26	1.78	0.79
Mainland China	0.94	0.03	3.79	0.96	0.79	-0.01	14.72	0.84	0.95	0.07	0.45	0.96	0.82	0.05	1.60	0.87
<i>The machine learning method: Gradient Boosting (GB)</i>																
NE	0.88	-0.12	3.92	0.92	0.77	0.06	13.94	0.83	0.93	-0.14	0.32	0.95	0.78	-0.09	1.36	0.84
NW	0.83	1.40	2.73	0.90	0.57	1.82	9.40	0.69	0.89	1.16	0.23	0.94	0.66	2.16	0.86	0.77
SW	-0.27	3.57	4.69	0.29	-0.59	5.92	12.86	0.14	0.17	4.33	0.33	0.65	-0.18	4.11	1.13	0.35
SE	0.82	-0.11	4.83	0.86	0.74	-0.13	13.41	0.8	0.89	-0.23	0.55	0.92	0.83	-0.26	1.46	0.87
Mainland China	0.92	-0.01	4.34	0.94	0.83	0.10	13.30	0.87	0.95	-0.08	0.44	0.96	0.88	-0.05	1.36	0.91

532

533 3.4 The regionalized IDF curves in Mainland China

534 Figure 6 shows the spatial distribution of four cases predicted by KED_AP and GB. Both
535 methods reveal a spatial pattern with a decreasing trend from the southeastern coastal areas to
536 the northwestern ~~interiorland~~, with overall similar distributions. This distribution is consistent
537 across different durations and return periods, highlighting the influence of China's varied climatic
538 and topographic conditions. In the SE region, which is characterized by humid subtropical and
539 monsoon climates, higher extreme rainfall intensities are evident. This region experiences the
540 most intense rainfall due to its proximity to oceanic moisture sources, ~~the~~ frequent passage of
541 typhoons, and summer monsoon systems. The reduction in extreme rainfall intensity moving
542 inland reflects the weakening of moisture-laden winds as they traverse the country and
543 encounter various geographical barriers, such as the Tibetan Plateau. This trend aligns with
544 another study on design rainstorms with a 2-year return period and a 20-minute duration in China,
545 which shows significantly higher rainstorm amounts in the east compared to the west, and in the
546 south compared to the north (Shao & Liu, 2018). However, notable local differences between
547 both methods can be observed. The interpolated rainfall intensity appears smoother and more
548 uniform. In contrast, the machine learning method exhibits weaker local autocorrelation,
549 resulting in more abrupt spatial changes(Figure 6). Interpolation relies on distant stations, leading
550 to values that are closer to those observed at existing stations, producing a more homogeneous
551 spatial distribution. The machine learning method, however, is more influenced by local
552 geographical conditions, resulting in greater spatial heterogeneity and highlighting the diversity
553 of the terrain and climate.



554

555 **Figure 6.** Spatial distribution of predicted rainfall intensity (mm/h) predictions from KED_AP (the
 556 best interpolation method, (a)-(d)) and GB (the best machine learning method, (e)-(h)).

557

558

Notably, the machine learning method predicts local peaks in the southeastern edge of the SW region, which are not captured by the interpolation results (Figure 6). This discrepancy

559 was also found in comparisons of rainfall erosivity (i.e., the potential for water erosion caused by
560 rainfall) estimated ~~by with~~ Global Climate Models (GCM) generated rainfall and gauge-observed
561 hourly rainfall (Wang et al., 2023), which likely arises from the influence of orographic rainfall on
562 the windward slopes, leading to more extreme precipitation in this area. The machine learning
563 method can detect this feature from the grid data. In contrast, the interpolation method,
564 constrained by the sparse distribution of rain gauges, extrapolates the rainfall intensity from
565 surrounding areas with less rainfall, thereby missing this localized phenomenon. This underscores
566 the advantage of machine learning methods based on gridded precipitation data in regions where
567 station data is sparse or unavailable.

568 4 Discussion

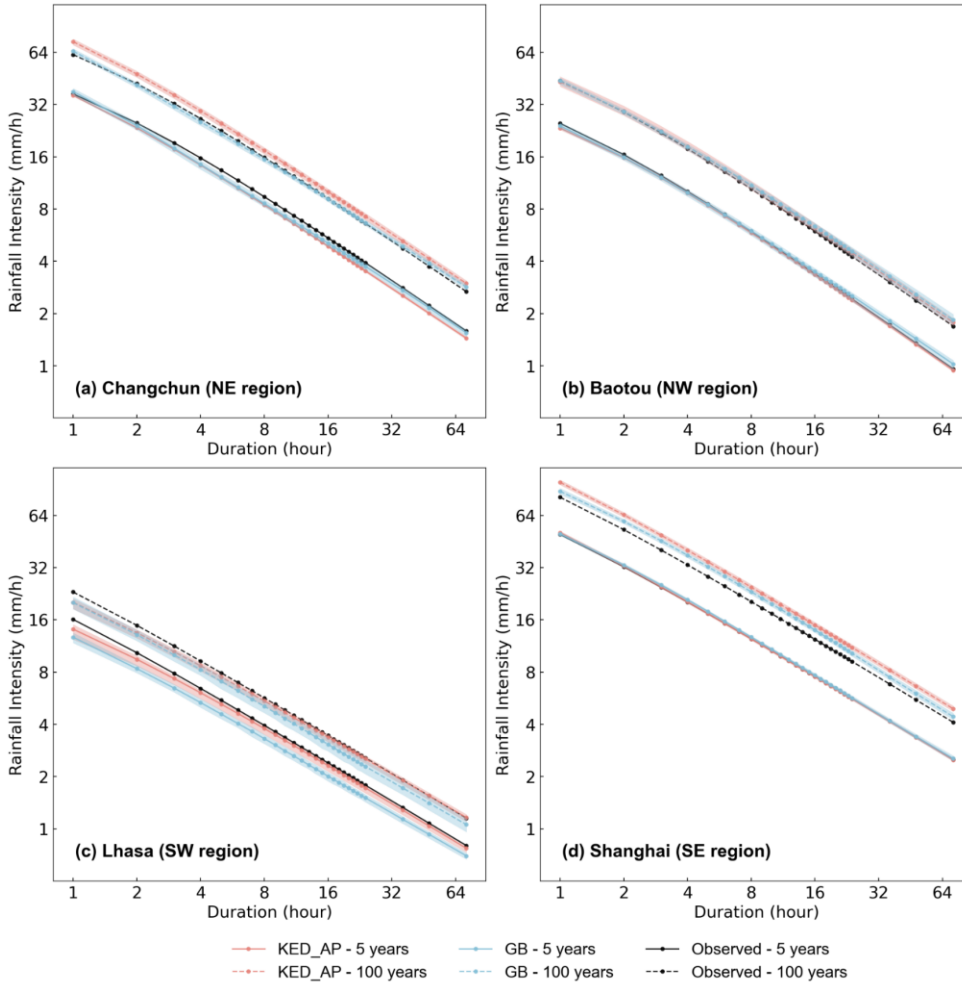
569 ~~Building on the results from the national and regional evaluations, the objective of this~~
570 ~~study was to comprehensively evaluate the~~ effectiveness of different regionalization methods
571 ~~was comprehensively evaluated in this study~~ for estimating regionalized IDF curves across
572 mainland China. Specifically, the IDF curves were regionalized using five traditional interpolation
573 methods—Inverse Distance Weighted (IDW), Ordinary Kriging (OK), Kriging with External Drift
574 using annual average precipitation (KED_AP), Kriging with External Drift using elevation
575 (KED_DEM), and Kriging with External Drift using both elevation and annual average precipitation
576 (KED_DEM+AP)—along with five different machine learning methods: Random Forest (RF),
577 Gradient Boosting (GB), Extremely Randomized Trees (ET), Multilayer Perceptron (MLP), and
578 Linear Regression (LR). To evaluate the accuracy, each regionalization method was compared
579 against site-specific IDF curves used as benchmarks. In addition, this study attempt~~eds~~ to test
580 whether any of the methods combined daily precipitation data could be satisfactorily used to
581 regionalize and extrapolate IDF curves for storm durations much shorter than 24 hours.

582 The comparison of interpolation and machine learning methods for IDF curves
583 ~~regionalization~~ across mainland China reveals several notable patterns and insights. Our analysis
584 demonstrates that both methods can effectively estimate extreme rainfall intensities, with the
585 best-performing methods from each category—KED_AP for interpolation and GB for machine
586 learning—achieving comparable accuracy levels. Furthermore, the relationship between
587 prediction accuracy and IDF cases exhibits clear patterns: both methods show decreased
588 performance with shorter durations and larger return periods. This pattern aligns with the
589 inherent challenges in predicting more extreme and temporally concentrated rainfall events.
590 KED_AP outperforms other interpolation methods, such as OK and KED_DEM, likely because ~~the~~
591 annual average precipitation ~~is aserves as a~~ more effective covariate for capturing the spatial
592 patterns of extreme rainfall across diverse terrains ~~compared to other covariates considered in~~
593 ~~this study~~. This advantage may stem from its strong correlation with extreme precipitation,
594 whereas elevation, despite some correlation with extreme precipitation in ~~regions of~~ complex
595 topography, appears less effective in flatter regions where its influence on extreme precipitation
596 diminishes (Zou et al., 2021). As for machine learning methods, ensemble learning techniques,
597 particularly GB, have demonstrated stable and excellent performance. ~~GB's effectiveness likely~~
598 ~~stems from its sequential boosting framework, which iteratively reduces residual errors by fitting~~
599 ~~each new model to the negative gradient of the loss function (Friedman, 2001). This process,~~
600 ~~combined with built-in regularization techniques, helps GB reduce overfitting and adaptively~~

601 ~~focus on difficult to predict instances, which may make it suitable for modeling extreme events.~~
602 To assess the interpretability of the GB model, a feature importance analysis using Shapley
603 Additive Explanations (Lundberg & Lee, 2017) was conducted (Figure S4). This analysis reveals
604 that the model's predictive power is primarily driven by features derived from the gridded
605 precipitation data characterizing daily extremes, specifically the gridded daily precipitation of
606 varying return periods and the average annual maximum daily precipitation. This is likely because
607 the model effectively learns the strong correlation between extreme precipitation events at sub-
608 daily scales and corresponding daily gridded precipitation extremes, capturing this shared
609 pattern across numerous samples through its non-linear capabilities. Furthermore, geographic
610 variables like latitude, longitude, and elevation consistently rank as important secondary features.
611 These variables establish the background precipitation gradient controlled by climatic and
612 topographic factors across mainland China. This spatial baseline, ~~together integrated~~ with daily
613 extreme precipitation features, enables the model to produce spatially heterogeneous IDF
614 estimations.

615 The national-level analysis, however, raises an important question about the spatial
616 consistency of these findings. While both methods demonstrate robust overall performance,
617 their effectiveness may vary across the ~~study area's~~ diverse geographical and climatic regions in
618 mainland China. This consideration is particularly relevant given the country's complex
619 topography and rainfall patterns. Therefore, it is essential to examine how these methods
620 perform across different regions. The analysis in Section 3.3 reveals that both methods achieve
621 acceptable accuracy in the NE, SE, and NW regions, while in the SW region, both methods show
622 reduced performance, with the machine learning method exhibiting lower accuracy than the
623 interpolation method (Table 4). Figure 7 further illustrates ~~partial~~ IDF curves from representative
624 stations in in each of the four regions, indicating that both the interpolation and machine learning
625 methods produce IDF curves with low uncertainty and high consistency with observed curves.
626 This further corroborates the reliability of both methods. The performance discrepancy between
627 the interpolation and machine learning methods in the SW region is likely because, despite the
628 overall lower station density and complex terrain in the SW region, the training and validation
629 stations are relatively concentrated, thereby reducing the limitations imposed by station density
630 on interpolation accuracy (Figure 1). This suggests that the interpolation method may exhibit
631 reduced predictive accuracy in the western areas of the SW region, where validation stations are
632 sparsely distributed, although this conclusion cannot be confirmed due to the absence of
633 observational data for verification. In comparison, the accuracy of the machine learning method
634 is more constrained by the availability of local samples. The machine learning model, trained on
635 national station data, cannot accurately capture the unique rainfall patterns in the SW region due
636 to the limited number of local training stations there. In addition, the representativeness errors
637 inherent in gridded precipitation data could further impair the machine learning method's
638 predictive accuracy in this region.

639



640

641

642

643

644

645

646

647

648

649

650

651

652

653

654

655

656

657

Figure 7 IDF curves ~~using based on~~ KED_AP (interpolation method), GB (machine learning method), and observed data for (a) Changchun in the NE region, (b) Baotou in the NW region, (c) Lhasa in the SW region, and (d) Shanghai in the SE region, with return periods of 5 and 100 years. For all stations in the mainland China except the four shown, 80% were randomly selected as training samples for both interpolation and machine learning methods, with this process repeated 500 times ~~using Monte Carlo sampling~~ to predict the IDF curves for these ~~four displayed~~ stations. Black lines represent the observed IDF curves, ~~r~~Red lines represent the mean of the 500 samples for the interpolation method, and blue lines represent the mean for the machine learning method, with solid lines indicating the 5-year return period and dashed lines indicating the 100-year return period. Shaded areas correspond to the 2.5th and 97.5th percentiles of the 500 samples.

A particularly interesting finding is the gradual shift ~~with duration and return period~~ in relative performance between the two methods ~~evaluated as duration and return period change~~. As duration and return period increase, the accuracy of machine learning in most regions gradually improves, eventually approaching or even surpassing the interpolation, consistent with the national evaluation (Table 4 and Figure 3). The enhanced relative performance of machine

658 learning methods for longer durations may be attributed to the disparity in the temporal
659 resolution of the independent variables (Table 1). Specifically, the interpolation utilizes station
660 rainfall data with higher temporal resolution (hourly), whereas the machine learning relies on
661 daily gridded precipitation data. Consequently, the accuracy of the interpolation remains
662 relatively unaffected by shorter durations, whereas machine learning exhibits reduced predictive
663 capability for short-duration rainfall events but demonstrates its inherent predictive advantages
664 for long-duration rainfall. This suggests that utilizing gridded precipitation data with higher
665 temporal resolution as independent variables would likely lead to improved accuracy in
666 regionalized IDF curves based on machine learning. Furthermore, the enhanced relative
667 performance of machine learning methods for larger return periods may stem from their ability
668 to better handle extreme rainfall events, where the assumptions of spatial autocorrelation
669 required by interpolation methods become less tenable. Machine learning models make better
670 use of local precipitation and topographical features, allowing/enabling them to capture the
671 complex non-linear relationships between these features and extreme rainfall more effectively
672 than interpolation methods.

673 Further practical differences between interpolation and machine learning methods were
674 identified that generally apply in various contexts. The machine learning approach is useful in
675 applications where a trained model may be used to make predictions for areas with observations
676 surfaces without having observation points with known values. This means that machine learning
677 is particularly useful for forecasting of future prediction surfaces, while in contrast, forecasting is
678 not possible with interpolation techniques that always require point observations/points. By
679 comparison, interpolation techniques may be preferable for producing prediction surfaces for
680 historical time frames where observations are available. The geospatial approach used
681 by most interpolation methods considers data in the surrounding neighborhood of the point for
682 prediction/datapoint. Consequently, interpolation methods may be expected to result in
683 smoother surfaces with a higher degree of spatial autocorrelation compared to the test machine
684 learning methods that only consider information where prediction is attempted/at the exact
685 datapoint being predicted. Therefore, the choice of prediction method may depend on the
686 context of the application and the available data.

687 Several limitations regarding data availability and methodological assumptions should be
688 noted. While our study/Notably, while our study found that the accuracies of machine learning
689 and interpolation accuracies are comparable, this conclusion may change as more validation
690 stations are included. For instance, given that interpolation accuracy is constrained by station
691 density, large areas in the NW and SW regions both lack stations and are distant from existing
692 stations (Figure 1), likely resulting in severely affected interpolation accuracy in these areas.
693 Similarly, since the accuracy of machine learning is constrained by the availability of non-local
694 samples, and the gridded precipitation datasets in these regions may have been significantly
695 underestimated ion (Miao et al., 2024), the results derived from machine learning based on these
696 datasets may also be severely affected. Due to the lack of stations for verification, these remain
697 unconfirmed and will need to be validated with installation of additional/by establishing more
698 stations in the future. It is also important to note that, although regionalized IDF were generated
699 for the NW and SW regions in this study, their use should be approached with caution due to the
700 lack of station-based verification. Users are strongly advised to consider the higher uncertainty

701 associated with predictions in these areas and validate results against local observations if
702 available. For the SW region, an alternative high-resolution IDF dataset ($1/30^\circ$) trained with local
703 samples offers a valuable supplement to our work (Ren et al., 2025). While our study focuses on
704 the robustness and general applicability of regionalization methods at a near-national scale
705 across diverse climates and topographies, their study concentrates on achieving high-resolution
706 regionalization within one of the most complex regions in mainland China. Another limitation
707 worth noting is that our study employed stationary IDF curves derived from historical
708 observations, assuming temporal invariance in the extreme precipitation distribution. ~~With Given~~
709 ~~that climate change is expected to increase~~ both the frequency and intensity of extreme
710 ~~precipitation events are expected to increase~~, thereby affecting the distributional parameters,
711 future studies should investigate how these regionalization methods perform under non-
712 stationary conditions. Furthermore, limitations inherent in the observational records must be
713 acknowledged, specifically the uncertainty associated with extrapolating 10-70 years of records
714 to 1000-year return periods, and the exclusion of sub-hourly events due to the minimum input
715 duration of one hour.

716
717
718 Finally~~Additionally~~, this study not only highlights the promise of machine learning but also
719 points to opportunities for further refinement. The potential for improving the accuracy of
720 interpolation methods in this study area is limited, due to the lack of higher station density and
721 finer temporal resolution observations. Conversely, machine learning methods have substantial
722 room for improvement through enhanced temporal and spatial resolution of gridded
723 precipitation data, improved data quality, incorporation of additional meteorological variables
724 such as temperature, relative humidity, and atmospheric circulation patterns, as well as the
725 development of more advanced machine learning techniques and exploration of more
726 comprehensive hyperparameter combinations not considered in this study~~as well as the~~
727 ~~development of more advanced machine learning techniques~~. Such advancements could
728 significantly improve the predictive capabilities beyond the results demonstrated in this study.

729 5 Conclusions

730 This study explored optimal methods for regionalizing Intensity-Duration-Frequency (IDF)
731 curves across mainland China, utilizing long-term hourly precipitation data from 2363
732 observation stations across mainland China, as well as daily gridded precipitation data from the
733 CHM_PRE. To achieve this objective, we evaluated and compared the performance of five
734 traditional interpolation methods (site-observation-based) and five emerging machine learning
735 methods (gridded-precipitation-based). Four representative rainfall intensities~~cases~~ were
736 selected as examples: 1-hour, 5-year rainfall intensity for a 5-year return period (SDSR), 1-hour,
737 100-year 1-hour rainfall intensity for a 100-year return period (SDLR), 24-hour, 5-year 24-hour
738 rainfall intensity for a 5-year return period (LDSR), and 24-hour, 100-year 24-hour rainfall intensity
739 for a 100-year return period (LDLR). The following key findings were obtained:

- 740 (1) Among all interpolation methods evaluated~~employed~~ in this study, Kriging methods
741 incorporating annual precipitation as a covariate (KED_AP) significantly improved

742 prediction accuracy compared with the Ordinary Kriging(OK), whereas including
743 elevation as a covariate did not improve the accuracy ~~or even reduced it~~. Among all
744 machine learning methods evaluated used in this study, Gradient Boosting (GB)
745 demonstrated the best and most robust performance.

746 (2) For the best-performing interpolation and machine learning methods across the four
747 ~~target~~-rainfall intensities selected, both methods demonstrated comparable and robust
748 performance across various cases, whether for short or long durations and return periods.
749 Specifically, the KED_AP method achieved a KGE of over 0.96 for SDSR and LDSR, and over
750 0.84 for SDLR and LDLR. Similarly, the GB method achieved a KGE of over 0.94 for SDSR
751 and LDSR, and over 0.87 for SDLR and LDLR. Machine learning methods tend to perform
752 relatively better as the duration and return period increase. Besides, shorter durations
753 and larger return periods were associated with increased prediction difficulty and
754 reduced accuracy for both methods, as evidenced by the KGE values for LDSR (KED_AP =
755 0.96; GB = 0.96) and SDLR (KED_AP = 0.84; GB = 0.87).

756 (3) IDF curves typically require precipitation data with sub-daily temporal resolution (e.g.,
757 hourly) when using traditional interpolation methods. In contrast, machine learning
758 methods, utilizing only daily precipitation data and not previously applied to IDF curves
759 regionalization in mainland China, demonstrated comparable accuracy to traditional
760 methods and even outperformed them for long durations and large return periods.
761 Additionally, machine learning offers distinct advantages, such as only requiring coarser
762 temporal resolution precipitation data, being independent of station setup conditions,
763 and possessing strong adaptability for future updates. These advantages suggest that
764 machine learning has the potential to replace interpolation methods to produce in-future
765 IDF curves ~~regionalization applications~~.

766 ~~With~~By determining the optimal regionalization method for each specific duration and
767 return period, the study ultimately produced a regionalized IDF curves product for mainland
768 China with a spatial resolution of $0.1^{\circ} \times 0.1^{\circ}$. The durations considered ranged from 1 to 24 hours,
769 along with 36, 48, and 72 hours, and the return periods included 2, 5, 10, 20, 50, 100, 200, 500,
770 and 1000 years. Although with lower accuracy, another IDF curves product for mainland China
771 with a spatial resolution of $0.5^{\circ} \times 0.5^{\circ}$ based on CGDPP, is also provided as an alternative. To
772 resolve potential crossing phenomena within the generated curves, a bivariate isotonic
773 regression was applied as post-processing, ensuring physical consistency with negligible impact
774 on accuracy (Dykstra, 1983). We also provided accuracy metrics and the name of the optimal
775 regionalization methods for each IDF case (Tables S31, S36, S41–S48)~~(Tables S18 to S27)~~. Taking
776 the city of Beijing (approximately 16,000 km²) as an example, the existing hourly gauges provide
777 about 20 station-level IDF curves. Our 0.1° dataset increases this to about 170 available IDF curves,
778 while the 0.5° dataset provides about 8 curves. The 0.1° dataset is recommended for local-scale
779 applications requiring high spatial detail, such as for urban drainage design and small catchment
780 flood modeling for example, while the 0.5° dataset is appropriate for ~~suits~~-regional-scale
781 hydrologic modeling where computational efficiency and areal-average representation are
782 prioritized.

In summary, this study advances regionalization of the field of IDF curves ~~regionalization~~ ~~by offering with~~ several distinct contributions that enhance both methodological understanding and practical application. First, through a systematic comparison of traditional interpolation and emerging machine learning methods, this research ~~highlights~~~~utilizes~~ the relative strengths of each method, enabling the identification of optimal regionalization strategies tailored to specific duration and return period combinations. Second, the study demonstrates that machine learning methods, using readily available gridded daily ~~scale~~ precipitation data, can estimate sub-daily IDF curves with accuracy comparable to traditional interpolation methods ~~using based on~~ hourly data. This finding is particularly significant~~meaningful~~ for regions where high-temporal-resolution data are scarce, as it expands the potential for effective IDF regionalization in data-limited environments. Third, by generating a regionalized dataset on IDF curves ~~dataset~~ for mainland China where such datasets were previously scarce, this study has generated~~ds~~ a valuable resource for flood risk assessment and infrastructure planning, while ~~also~~ providing a valuable methodological framework for similar studies in other regions.

Appendix

Table A1. List of important acronyms and their definitions

<u>Acronym</u>	<u>Definition</u>
<u>ET</u>	<u>Extremely Randomized Trees</u>
<u>GB</u>	<u>Gradient Boosting</u>
<u>GEV</u>	<u>Generalized Extreme Value</u>
<u>IDF</u>	<u>Intensity-Duration-Frequency</u>
<u>IDW</u>	<u>Inverse Distance Weighting</u>
<u>KED</u>	<u>Kriging with External Drift</u>
<u>KED AP</u>	<u>Kriging with External Drift using Mean Annual Precipitation</u>
<u>KED DEM</u>	<u>Kriging with External Drift using Elevation</u>
<u>KGE</u>	<u>Kling-Gupta Efficiency</u>
<u>LDLR</u>	<u>Long Duration-Large Return Period</u>
<u>LDSR</u>	<u>Long Duration-Small Return Period</u>
<u>LR</u>	<u>Linear Regression</u>
<u>ML</u>	<u>Machine Learning</u>
<u>MLP</u>	<u>Multilayer Perceptron</u>
<u>NE</u>	<u>Northeastern Monsoon Region</u>
<u>NSE</u>	<u>Nash-Sutcliffe Efficiency</u>
<u>NW</u>	<u>Northwestern Arid Region</u>

<u>OK</u>	<u>Ordinary Kriging</u>
<u>PBIAS</u>	<u>Percent Bias</u>
<u>RF</u>	<u>Random Forest</u>
<u>RMSE</u>	<u>Root Mean Square Error</u>
<u>SDLR</u>	<u>Short Duration-Large Return Period</u>
<u>SDSR</u>	<u>Short Duration-Small Return Period</u>
<u>SE</u>	<u>Southeastern Monsoon Region</u>
<u>SW</u>	<u>Southwestern Tibetan Plateau Region</u>

800

801

802 **Author contribution**

803 YJ developed the methodology, performed the ~~data~~formal analysis, created the visualizations,
 804 and wrote the original draft; [WW conceptualized and designed the study, provided the data](#)
 805 [and initial scripts, acquired the funding, and supervised the project; WW and YJ revised the](#)
 806 [original draft; All authors commented, reviewed and edited the manuscript.~~WW conceptualized~~
 807 ~~the study, collected the data, and administered the project; WW and YJ revised the original~~
 808 ~~draft; All authors commented, reviewed and edited the final manuscript.~~](#)

809

810 **Acknowledgments**

811 This work was supported by the National Natural Science Foundation of China (No.42307424),
 812 and State Key Laboratory of Earth Surface Processes and Resource Ecology (2023-KF-10). [We](#)
 813 [thank Zeng He for helping prepare the scripts.](#) The authors utilized the AI model DeepSeek-R1
 814 [\(Guo et al., 2025\)](#) to enhance the language of this manuscript. The tool was employed solely for

815 improving grammar, syntax, and word choice. The authors reviewed and revised all AI-generated
816 suggestions to ensure the scientific accuracy of the content.

817

818 **Data Availability Statement**

819 Regionalized Intensity-Duration-Frequency curves in mainland China (0.1°/0.5°) are available at
820 <https://data.tpdc.ac.cn/en/disallow/ba9c23d1-cdbf-471c-90d5-b413d2a9f86a>.

821

822 **Competing interests**

823 The authors declare that they have no known competing financial interests or personal
824 relationships that could have appeared to influence the work reported in this paper.

825

826 **References**

827 Al Kajbaf, A., Bensi, M., & Brubaker, K. L. (2022). Temporal downscaling of precipitation from
828 climate model projections using machine learning. *Stochastic Environmental Research and
829 Risk Assessment*, 36(8), 2173–2194. <https://doi.org/10.1007/s00477-022-02259-2>

830 Al Kajbaf, A., Bensi, M., & Brubaker, K. L. (2023). Drivers of uncertainty in precipitation
831 frequency under current and future climate – application to Maryland, USA. *Journal of
832 Hydrology*, 617, 128775. <https://doi.org/10.1016/j.jhydrol.2022.128775>

833 Armstrong, M. (1998). *Basic linear geostatistics*. Berlin, Heidelberg: Springer-Verlag.
834 <https://doi.org/10.1007/978-3-642-58727-6>

835 Benestad, R. E., Lutz, J., Dyrddal, A. V., Haugen, J. E., Parding, K. M., & Dobler, A. (2021). Testing a
836 simple formula for calculating approximate intensity-duration-frequency curves.
837 *Environmental Research Letters*, 16(4), 044009. [https://doi.org/10.1088/1748-
838 9326/abd4ab](https://doi.org/10.1088/1748-9326/abd4ab)

839 Berndt, C., & Haberlandt, U. (2018). Spatial interpolation of climate variables in Northern

840 Germany—Influence of temporal resolution and network density. *Journal of Hydrology:*
841 *Regional Studies*, 15, 184–202. <https://doi.org/10.1016/j.ejrh.2018.02.002>

842 Berndt, C., Rabiei, E., & Haberlandt, U. (2014). Geostatistical merging of rain gauge and radar
843 data for high temporal resolutions and various station density scenarios. *Journal of*
844 *Hydrology*, 508, 88–101. <https://doi.org/10.1016/j.jhydrol.2013.10.028>

845 Breiman, L. (2001). Random forests. *Machine Learning*, 45, 5–32.
846 <https://doi.org/10.1023/A:1010933404324>

847 Courty, L. G., Wilby, R. L., Hillier, J. K., & Slater, L. J. (2019). Intensity-duration-frequency curves
848 at the global scale. *Environmental Research Letters*, 14(8), 084045.
849 <https://doi.org/10.1088/1748-9326/ab370a>

850 Donat, M. G., Alexander, L. V., Herold, N., & Dittus, A. J. (2016). Temperature and precipitation
851 extremes in century-long gridded observations, reanalyses, and atmospheric model
852 simulations. *Journal of Geophysical Research: Atmospheres*, 121, 11,174–11,189.
853 <https://doi.org/10.1002/2016JD025480>

854 Dykstra, R. L. (1983). An algorithm for restricted least squares regression. *Journal of the*
855 *American Statistical Association*, 78(384), 837 – 842.
856 <https://doi.org/10.1080/01621459.1983.10477029>

857 Förster, K., & Thiele, L. B. (2020). Variations in sub-daily precipitation at centennial scale. *npj*
858 *Climate and Atmospheric Science*, 3(1), 13. <https://doi.org/10.1038/s41612-020-0117-1>

859 Friedman, J. H. (2001). Greedy Function Approximation: A Gradient Boosting Machine. *The*
860 *Annals of Statistics*, 29(5), 1189–1232. <http://www.jstor.org/stable/2699986>

861 Funk, C., Peterson, P., Landsfeld, M., Pedreros, D., Verdin, J., Shukla, S., Husak, G., Rowland, J.,
862 Harrison, L., Hoell, A., & Michaelsen, J. (2015). The climate hazards infrared precipitation
863 with stations—A new environmental record for monitoring extremes. *Scientific Data*, 2(1),
864 150066. <https://doi.org/10.1038/sdata.2015.66>

865 Gao, L., Huang, J., Chen, X., Chen, Y., & Liu, M. (2017). Risk of Extreme Precipitation under
866 Nonstationarity Conditions during the Second Flood Season in the Southeastern Coastal
867 Region of China. *Journal of Hydrometeorology*, 18(3), 669–681.
868 <https://doi.org/10.1175/JHM-D-16-0119.1>

869 Gaur, A., Schardong, A., & Simonovic, S. P. (2020). Gridded Extreme Precipitation Intensity-
870 Duration-Frequency Estimates for the Canadian Landmass. *JOURNAL OF HYDROLOGIC*
871 *ENGINEERING*, 25(6), 05020006. [https://doi.org/10.1061/\(ASCE\)HE.1943-5584.0001924](https://doi.org/10.1061/(ASCE)HE.1943-5584.0001924)

872 Geurts, P., Ernst, D., & Wehenkel, L. (2006). Extremely randomized trees. *Machine learning*, 63,
873 3-42. <https://doi.org/10.1007/s10994-006-6226-1>

874 Ghebreyesus, D. T., & Sharif, H. O. (2021). Development and Assessment of High-Resolution
875 Radar-Based Precipitation Intensity-Duration-Curve (IDF) Curves for the State of Texas.
876 *Remote Sensing*, 13(15), 2890. <https://doi.org/10.3390/rs13152890>

877 [Guo, D., Yang, D., Zhang, H., Song, J., Wang, P., Zhu, Q., Xu, R., Zhang, R., Ma, S., Bi, X., Zhang, X.,](#)
878 [Yu, X., Wu, Y., Wu, Z. F., Gou, Z., Shao, Z., Li, Z., Gao, Z., Liu, A., ... Zhang, Z. \(2025\).](#)
879 [DeepSeek-R1 incentivizes reasoning in LLMs through reinforcement learning. *Nature*,](#)
880 [645\(8081\), 633–638. <https://doi.org/10.1038/s41586-025-09422-z>](#)

881 Halbert, K., Nguyen, C. C., Payraastre, O., & Gaume, E. (2016). Reducing uncertainty in flood
882 frequency analyses: A comparison of local and regional approaches involving information
883 on extreme historical floods. *Journal of Hydrology*, 541, 90–98.
884 <https://doi.org/10.1016/j.jhydrol.2016.01.017>

885 Han, J., Miao, C., Gou, J., Zheng, H., Zhang, Q., & Guo, X. (2023). A new daily gridded
886 precipitation dataset for the Chinese mainland based on gauge observations. *Earth System*
887 *Science Data*, 15(7), 3147–3161. <https://doi.org/10.5194/essd-15-3147-2023>

888 Haruna, A., Blanchet, J., & Favre, A. (2024). Estimation of Intensity-Duration-Area-Frequency
889 Relationships Based on the Full Range of Non-Zero Precipitation From Radar-Reanalysis
890 Data. *Water Resources Research*, 60(2), e2023WR035902.
891 <https://doi.org/10.1029/2023WR035902>

892 Hinton, G. E. (1989). Connectionist learning procedures. *Artificial Intelligence*, 40(1-3), 185-234.
893 [https://doi.org/10.1016/0004-3702\(89\)90049-0](https://doi.org/10.1016/0004-3702(89)90049-0)

894 Hosking, J.R.M. (1990). L-moments: Analysis and estimation of distributions using linear
895 combinations of order statistics. *Journal of the Royal Statistical Society: Series B*
896 *(Methodological)*, 52(1), 105–124. <https://doi.org/10.1111/j.2517-6161.1990.tb01775.x>

897 Jenkinson, A. F. (1955). The frequency distribution of the annual maximum (or minimum) values

898 of meteorological elements. *Quarterly Journal of the Royal Meteorological Society*,
899 81(348), 158–171. <https://doi.org/10.1002/qj.49708134804>

900 Koutsoyiannis, D., Kozonis, D., & Manetas, A. (1998). A mathematical framework for studying
901 rainfall intensity-duration-frequency relationships. *Journal of Hydrology*, 206(1–2), 118–
902 135. [https://doi.org/10.1016/S0022-1694\(98\)00097-3](https://doi.org/10.1016/S0022-1694(98)00097-3)

903 Lanciotti, S., Ridolfi, E., Russo, F., & Napolitano, F. (2022). Intensity-Duration-Frequency Curves in
904 a Data-Rich Era: A Review. *Water*, 14(22), 3705. <https://doi.org/10.3390/w14223705>

905 Li, J., & Heap, A. D. (2008). *A review of spatial interpolation methods for environmental*
906 *scientists*. Canberra, Australia: Geoscience Australia.

907 Li, J., Yu, R., Yuan, W., & Chen, H. (2011). Changes in Duration-Related Characteristics of Late-
908 Summer Precipitation over Eastern China in the Past 40 Years. *Journal of Climate*, 24(21),
909 5683–5690. <https://doi.org/10.1175/JCLI-D-11-00009.1>

910 [Lundberg, S. M., & Lee, S.-I. \(2017\). A unified approach to interpreting model predictions. In I.](#)
911 [Guyon, U. V. Luxburg, S. Bengio, H. Wallach, R. Fergus, S. Vishwanathan, & R. Garnett](#)
912 [\(Eds.\), *Advances in Neural Information Processing Systems* \(Vol. 30, pp. 4765–4774\).](#)

913 Maggioni, V., & Massari, C. (Eds.). (2019). *Extreme Hydroclimatic Events and Multivariate*
914 *Hazards in a Changing Environment*. Amsterdam, Netherlands: Elsevier.
915 <https://doi.org/10.1016/B978-0-12-814899-0.00016-X>

916 Miao, C., Immerzeel, W. W., Xu, B., Yang, K., Duan, Q., & Li, X. (2024). Understanding the Asian
917 water tower requires a redesigned precipitation observation strategy. *Proceedings of the*
918 *National Academy of Sciences*, 121(23), e2403557121.
919 <https://doi.org/10.1073/pnas.2403557121>

920 Mínguez, R., & Herrera, S. (2023). Spatial extreme model for rainfall depth: Application to the
921 estimation of IDF curves in the Basque country. *Stochastic Environmental Research and*
922 *Risk Assessment*, 37(8), 3117–3148. <https://doi.org/10.1007/s00477-023-02440-1>

923 [Mockus, J., Tiesis, V., & Žilinskas, A. \(1978\). The application of Bayesian methods for seeking the](#)
924 [extremum. In L. C. W. Dixon & G. P. Szegő \(Eds.\), *Towards global optimisation* \(Vol. 2, pp.](#)
925 [117–129\).](#)

926 Nguyen, V.-T.-V., Nguyen, T.-D., & Ashkar, F. (2002). Regional frequency analysis of extreme

927 rainfalls. *Water Science and Technology*, 45(2), 75–81.
928 <https://doi.org/10.2166/wst.2002.0030>

929 Noor, M., Ismail, T., Shahid, S., Asaduzzaman, M., & Dewan, A. (2021). Evaluating intensity-
930 duration-frequency (IDF) curves of satellite-based precipitation datasets in Peninsular
931 Malaysia. *Atmospheric Research*, 248, 105203.
932 <https://doi.org/10.1016/j.atmosres.2020.105203>

933 Papalexiou, S. M. (2018). Unified theory for stochastic modelling of hydroclimatic processes:
934 Preserving marginal distributions, correlation structures, and intermittency. *Advances in*
935 *Water Resources*, 115, 234–252. <https://doi.org/10.1016/j.advwatres.2018.02.013>

936 Papalexiou, S. M., & Koutsoyiannis, D. (2013). Battle of extreme value distributions: A global
937 survey on extreme daily rainfall. *Water Resources Research*, 49(1), 187–201.
938 <https://doi.org/10.1029/2012WR012557>

939 Parding, K. M., Benestad, R. E., Dyrddal, A. V., & Lutz, J. (2023). A principal-component-based
940 strategy for regionalisation of precipitation intensity-duration-frequency (IDF) statistics.
941 *HYDROLOGY AND EARTH SYSTEM SCIENCES*, 27(20), 3719–3732.
942 <https://doi.org/10.5194/hess-27-3719-2023>

943 Pebesma, E. J. (2004). Multivariable geostatistics in S: the gstat package. *Computers &*
944 *geosciences*, 30(7), 683-691. <https://doi.org/10.1016/j.cageo.2004.03.012>

945 Pedregosa, F., Varoquaux, G., Gramfort, A., Michel, V., Thirion, B., Grisel, O., ... & Duchesnay, É.
946 (2011). Scikit-learn: Machine learning in Python. *Journal of machine Learning research*, 12,
947 2825-2830. <https://doi.org/10.48550/arXiv.1201.0490>

948 Ren, Z., Sang, Y.-F., Cui, P., Chen, F., & Chen, D. (2025). A dataset of gridded precipitation
949 intensity-duration-frequency curves in Qinghai-Tibet Plateau. *Scientific Data*, 12(1), 3.
950 <https://doi.org/10.1038/s41597-024-04362-1>

951 Sangüesa, C., Pizarro, R., Ingram, B., Ibáñez, A., Rivera, D., García-Chevesich, P., Pino, J., Pérez, F.,
952 Balocchi, F., & Peña, F. (2023). Comparing Methods for the Regionalization of
953 Intensity–Duration–Frequency (IDF) Curve Parameters in Sparsely-Gauged and Ungauged
954 Areas of Central Chile. *Hydrology*, 10(9), 179. <https://doi.org/10.3390/hydrology10090179>

955 Schilcher, U., Brandner, G., & Bettstetter, C. (2017). Quantifying inhomogeneity of spatial point

956 patterns. *Computer Networks*, 115, 65–81. <https://doi.org/10.1016/j.comnet.2016.12.018>

957 Schlef, K. E., Kunkel, K. E., Brown, C., Demissie, Y., Lettenmaier, D. P., Wagner, A., Wigmosta, M.
958 S., Karl, T. R., Easterling, D. R., Wang, K. J., François, B., & Yan, E. (2023). Incorporating non-
959 stationarity from climate change into rainfall frequency and intensity-duration-frequency
960 (IDF) curves. *Journal of Hydrology*, 616, 128757.
961 <https://doi.org/10.1016/j.jhydrol.2022.128757>

962 Shao, D., & Liu, G. (2018). Up-to-date urban rainstorm intensity formulas considering spatial
963 diversity in China. *Environmental Earth Sciences*, 77, 541. [https://doi.org/10.1007/s12665-](https://doi.org/10.1007/s12665-018-7718-6)
964 [018-7718-6](https://doi.org/10.1007/s12665-018-7718-6)

965 Shehu, B., Willems, W., Stockel, H., Thiele, L.-B., & Haberlandt, U. (2023). Regionalisation of
966 rainfall depth–duration–frequency curves with different data types in Germany. *Hydrology
967 and Earth System Sciences*, 27(5), 1109–1132. <https://doi.org/10.5194/hess-27-1109-2023>

968 Shen, Y., Mingnong, F., Hongzheng, Z., & Feng, G. (2010). Interpolation Methods of China Daily
969 Precipitation Data. *Journal of Applied Meteorological Science*, 21(3), 279–286.
970 <https://doi.org/10.3969/j.issn.1001-7313.2010.03.003>.

971 Simonović, S. P. (2012). *Floods in a changing climate: Risk management*. Cambridge, UK:
972 Cambridge University Press.

973 Skliris, N., Zika, J. D., Nurser, G., Josey, S. A., & Marsh, R. (2016). Global water cycle amplifying at
974 less than the Clausius-Clapeyron rate. *Scientific Reports*, 6, 38752.
975 <https://doi.org/10.1038/srep38752>

976 [Snoek, J., Larochelle, H., & Adams, R. P. \(2012\). Practical Bayesian optimization of machine
977 learning algorithms. In F. Pereira, C. J. C. Burges, L. Bottou, & K. Q. Weinberger \(Eds.\),
978 *Advances in Neural Information Processing Systems \(Vol. 25, pp. 2951–2959\)*.](#)

979 Szolgay, J., Parajka, J., Kohnová, S., & Hlavčová, K. (2009). Comparison of mapping approaches of
980 design annual maximum daily precipitation. *Atmospheric Research*, 92(3), 289–307.
981 <https://doi.org/10.1016/j.atmosres.2009.01.009>

982 Verworn, A., & Haberlandt, U. (2011). Spatial interpolation of hourly rainfall – effect of
983 additional information, variogram inference and storm properties. *Hydrology and Earth
984 System Sciences*, 15(2), 569–584. <https://doi.org/10.5194/hess-15-569-2011>

985 Vinod, D., & Mahesha, A. (2024). Modeling nonstationary intensity-duration-frequency curves
986 for urban areas of India under changing climate. *Urban Climate*, 56, 102065.
987 <https://doi.org/10.1016/j.uclim.2024.102065>

988 Wambura, F. J. (2024). Using reanalysis precipitation data for developing intensity-duration-
989 frequency curves in a poorly gauged city. *Journal of Hydrology: Regional Studies*, 56,
990 102005. <https://doi.org/10.1016/j.ejrh.2024.102005>

991 Wang, W., Yin, S., Xie, Y., Nearing, M. A., Wang, W., Yin, S., Xie, Y., & Nearing, M. A. (2019).
992 Minimum Inter-Event Times for Rainfall in the Eastern Monsoon Region of China.
993 *Transactions of the ASABE*, 62(1), 9–18. <https://doi.org/10.13031/trans.12878>

994 Wang, W., Yin, S., He, Z., Chen, D., Wang, H., & Klik, A. (2023). Projections of rainfall erosivity in
995 climate change scenarios for mainland China. *CATENA*, 232, 107391.
996 <https://doi.org/10.1016/j.catena.2023.107391>

997 Westra, S., Fowler, H. J., Evans, J. P., Alexander, L. V., Berg, P., Johnson, F., Kendon, E. J.,
998 Lenderink, G., & Roberts, N. M. (2014). Future changes to the intensity and frequency of
999 short-duration extreme rainfall. *Reviews of Geophysics*, 52(3), 522–555.
1000 <https://doi.org/10.1002/2014RG000464>

1001 Yin, S., Wang, Z., Zhu, Z., Zou, X., & Wang, W. (2018). Using Kriging with a heterogeneous
1002 measurement error to improve the accuracy of extreme precipitation return level
1003 estimation. *Journal of Hydrology*, 562, 518–529.
1004 <https://doi.org/10.1016/j.jhydrol.2018.04.064>

1005 Zhang, B., Wang, S., Moradkhani, H., Slater, L., & Liu, J. (2022). A Vine Copula-Based Ensemble
1006 Projection of Precipitation Intensity–Duration–Frequency Curves at Sub-Daily to Multi-Day
1007 Time Scales. *Water Resources Research*, 58(11), e2022WR032658.
1008 <https://doi.org/10.1029/2022WR032658>

1009 Zhao, S. (1983). A new scheme for comprehensive physical regionalization in China. *Acta*
1010 *Geographica Sinica*, 38(1), 1–10.

1011 Zou, W., Yin, S., & Wang, W. (2021). Spatial interpolation of the extreme hourly precipitation at
1012 different return levels in the Haihe River basin. *Journal of Hydrology*, 598, 126273.
1013 <https://doi.org/10.1016/j.jhydrol.2021.126273>

